The Propagation of the Gravity Current of Bingham Fluid

A Numerical Investigation

by

Ye Liu

B.Sc., Peking University, 2012

A THESIS SUBMITTED IN PARTIAL FULFILLMENT OF
THE REQUIREMENTS FOR THE DEGREE OF

MASTER OF SCIENCE

in

The Faculty of Graduate and Postdoctoral Studies

(Mathematics)

THE UNIVERSITY OF BRITISH COLUMBIA

(Vancouver)

December 2014

© Ye Liu 2014

Abstract

We have studied the propagation of 2D unit block of viscoplastic fluid of Bingham type over a horizontal plane, underneath another Newtonian fluid. We numerically simulate the dynamics of a two-layer fluid in a rectangle domain, using the volume-of-fluid method to deal with the evolution of the interface, and regularization scheme of the constitutive law, which replaces unyielded plugs with very viscous flow. We explore the final shape of the flow for varying yield stress, comparing the numerical results with the predictions of the asymptotic theory, a plasticity model based on slipline theory, and other past results. Numerical difficulties with the moving contact lines are encountered during the numerical simulation. A slip boundary condition is used to address this issue, the validity of which should be further investigated.

Preface

This thesis is original, unpublished, independent work by the author, Ye Liu.

Table of Contents

Abstract ii

Preface iii

Table of Contents iv

List of Figures vi

Acknowledgements ix

Dedication x

1 Introduction 1
- 1.1 Motivation 1
- 1.2 Literature review 2
- 1.3 Objectives 3

2 Problem Description 4
- 2.1 Problem setting 4
- 2.2 Equations 5
- 2.3 Dimensionless form 6

3 Asymptotic Results 7
- 3.1 A Newtonian two-layer model 7
- 3.2 A Bingham-Newtonian two-layer model 9
- 3.3 Final shape from plasticity theory 13
- 3.4 Relations of slump and aspect ratio 13

4 Numerical Results 16
4.1 Numerical scheme 16
4.1.1 Regularization method for Navier-Stokes equations . 17
4.1.2 Augmented Lagrangian method for Navier-Stokes equations 19
4.1.3 Algorithm for advection-diffusion equation 20
4.2 Parameter settings 22
4.3 Numerical result for Newtonian fluid problem 23
4.4 The no-slip boundary condition 27
4.5 Discussion about the result 36
4.6 Numerical result for Bingham fluid problem 37

5 Conclusion 46

Bibliography 48

Appendices

A Code Validation 51
A.1 The results are independent of tolerance 51
A.2 The results are independent of time step 51
A.3 The domain size 52
A.4 The density and viscosity ratio 53
A.5 Reynolds number 53
A.6 Regularization parameter is small enough 53
A.7 Problems with the slip boundary condition 54

List of Figures

2.1 problem setting 4

3.1 final shape for B=0.02 to 0.3 by 1-order shallow layer model . 14
3.2 final shape for B=0.02 to 0.2 by slipline model 14

4.1 upwind scheme 21
4.2 MUSCL scheme 22
4.3 flow profile for $T = 10, 40, 90, 160, 250,\ \frac{\mu_2}{\mu_1} = \frac{\rho_2}{\rho_1} = 10^{-3},\ Re = 9.81 \times 10^{-4}$ 24
4.4 x vs t for different resolution, $\frac{\mu_2}{\mu_1} = \frac{\rho_2}{\rho_1} = 10^{-3},\ Re = 9.81 \times 10^{-4}$ 25
4.5 h vs t for different resolution, $\frac{\mu_2}{\mu_1} = \frac{\rho_2}{\rho_1} = 10^{-3},\ Re = 9.81 \times 10^{-4}$ 25
4.6 concentration profile at $T = 250,\ \frac{\mu_2}{\mu_1} = \frac{\rho_2}{\rho_1} = 10^{-3},\ Re = 9.81 \times 10^{-4}$ 26
4.7 details about the concentration layer on the bottom 26
4.8 horizontal velocity at $x = 3.5,\ T = 250$, there is evident discontinuity in velocity field 27
4.9 numerical scheme around the boundary, stress in the grid cell is interpolated by velocity at the vertex 28
4.10 no-slip condition problem, $T = 10, 40, 90, 160, 250,\ \frac{\mu_2}{\mu_1} = \frac{\rho_2}{\rho_1} = 10^{-1},\ Re = 9.81 \times 10^{-4}$ 29
4.11 Navier slip boundary condition, $T = 10, 40, 90, 160, 250,\ \frac{\mu_2}{\mu_1} = \frac{\rho_2}{\rho_1} = 10^{-1},\ Re = 9.81 \times 10^{-4}$ 30
4.12 horizontal velocity at x=3.5, from Navier slip condition . . . 31
4.13 flow profile comparison of no-slip condition, Navier slip condition, modified slip condition, at the same time step, $T = 250,\ \frac{\mu_2}{\mu_1} = \frac{\rho_2}{\rho_1} = 10^{-1},\ Re = 9.81 \times 10^{-4}$ 32

4.14 details about the finger, $T = 250$, $\frac{\mu_2}{\mu_1} = \frac{\rho_2}{\rho_1} = 10^{-1}$, $Re = 9.81 \times 10^{-4}$ 32
4.15 horizontal velocity at x=3.5, from modified slip condition, the velocity is continuous and converges well 33
4.16 x vs t for modified slip model, $\frac{\mu_2}{\mu_1} = \frac{\rho_2}{\rho_1} = 10^{-1}$, $Re = 9.81 \times 10^{-4}$ 34
4.17 h vs t for modified slip model, $\frac{\mu_2}{\mu_1} = \frac{\rho_2}{\rho_1} = 10^{-1}$, $Re = 9.81 \times 10^{-4}$ 34
4.18 flow length vs time for different models, $\frac{\mu_2}{\mu_1} = \frac{\rho_2}{\rho_1} = 10^{-1}$, $Re = 9.81 \times 10^{-4}$ 35
4.19 flow height vs time for different models, $\frac{\mu_2}{\mu_1} = \frac{\rho_2}{\rho_1} = 10^{-1}$, $Re = 9.81 \times 10^{-4}$ 35
4.20 modified slip boundary condition, $T = 10, 40, 90, 160, 250$, $\frac{\mu_2}{\mu_1} = \frac{\rho_2}{\rho_1} = 10^{-1}$, $Re = 9.81 \times 10^{-4}$, white curves are from the two-layer shallow layer model 36
4.21 final shapes for different B 39
4.22 equilibrium flow length for B in [0.02 0.1] 41
4.23 equilibrium flow height for B in [0.02 0.1] 41
4.24 The color contour map is the stress field of the equilibrium state for B=0.02, the black curve is the 1-order shallow layer model 42
4.25 equilibrium flow length for B in [0.1 0.2] 43
4.26 equilibrium flow height for B in [0.1 0.2] 44
4.27 The color contour map is the stress field of the equilibrium state for B=0.2, the white curve is the slipline result 45

A.1 x vs t for different tolerance 51
A.2 h vs t for different tolerance 51
A.3 x vs t for different time step 52
A.4 h vs t for different time step 52
A.5 x vs t for different domain size 52
A.6 h vs t for different domain size 52
A.7 x vs t for different viscosity ratio 53
A.8 h vs t for different viscosity ratio 53
A.9 x vs t for different Reynolds number 54

A.10 h vs t for different Reynolds number 54
A.11 flow length vs time for different BCs 55

Acknowledgements

I would like to convey my gratitude to all people who gave me the possibility to complete this thesis. In the first place, I would like to express my sincere gratitude to my supervisor, Professor Neil Balmforth for the continuous support of my MSc study and research, for his patience, motivation, enthusiasm, and immense knowledge. His wide knowledge and his logical way of thinking have been of great value to me. I am deeply grateful to Professor Sarah Hormozi for her supervision, advice, and guidance from the early stage of this research. Above all and the most needed, they provided me support and friendly help in various ways. I would like to thank Mr Anthony Wachs, for assisting me with the validation of the numerical codes and Professor James Feng for useful advice. Most importantly, I would like to thank my entire family. My immediate family to whom this dissertation is dedicated, has been a constant source of love, concern, support and strength all these years. I would like to express my heart-felt gratitude to my parents who have supported and encouraged me throughout this endeavor. Finally, financial support of the Natural Sciences and Engineering Research Council of Canada (NSERC) is gratefully acknowledged.

Dedication

To my wonderful parents, who stood by me and supported all my ideas and dreams. I love you dearly. To my best friends in all aspects of my life, who have been by my side throughout difficult time. Your constant support and encouragement continue to help me reach my goals. I am forever thankful to have you in my life.

Chapter 1

Introduction

1.1 Motivation

A Bingham plastic is a viscoplastic material that behaves as a rigid body at low stress but flows as a viscous fluid at high stress. Unlike Newtonian fluid in which the viscous stress τ is linearly proportional to the strain rate γ, with a viscosity coefficient μ, the Bingham fluid satisfies the following constitutive law:

$$\begin{cases} \gamma = 0 & \boldsymbol{\tau} < \tau_y \\ \tau = \left(\mu + \dfrac{\tau_y}{\boldsymbol{\gamma}}\right)\gamma & \boldsymbol{\tau} > \tau_y \end{cases}$$

where τ_y is a scalar called the yield stress, $\boldsymbol{\tau} = \sqrt{\frac{1}{2}\tau : \tau}$ is the second invariant of the stress tensor τ, and $\boldsymbol{\gamma} = \sqrt{\frac{1}{2}\gamma : \gamma}$ is the second invariant of the strain rate tensor γ. When $\boldsymbol{\tau} < \tau_y$, the strain rate is zero, meaning that there is no local deformation. When $\boldsymbol{\tau} > \tau_y$, there is a linear relationship that $\boldsymbol{\tau} - \tau_y = \mu\boldsymbol{\gamma}$.

Bingham type plasticity is commonly used as a mathematical model for complex fluid in industry, such as drilling mud, concrete rheology, and food processing[16]. In those industries, the dynamic of gravity-driven flow plays an important role in a number of processes, including methods designed to measure fluid rheology. For example, the slump test is a way of measuring the consistency of fresh concrete. Furthermore, natural phenomenon like avalanche and debris flows can be modeled as a gravity flow of Bingham plastic[5]. A common feature of those phenomenon is that due to the yield criteria, the fluid will stop spreading as the stress fall below the yield stress, and form certain steady shape, instead of just continually flattening itself

like Newtonian fluid on scales long enough that surface tension is negligible. Therefore it is interesting to know what is the final shape of the fluid, and its relation with varying yield stress.

1.2 Literature review

For Newtonian fluid, the viscous gravity current of a single fluid has been well studied by Huppert[7] and others (see Bankoff et al [1]). Numerical tests for low Reynolds number flow, however, have rarely been implemented to validate the lubrication theory.

For Non-Newtonian fluid, a thin layer theory for Bingham-type fluid has been developed by Liu and Mei[12], based on Reynolds' lubrication theory. This theory leads to a prediction of the final shape in the shallow limit (see Balmforth, Craster and Sassi[21]). For non-shallow slumps, slipline theory from plasticity theory [2] has been applied to predict the final shape, by Dubash et al[20].

For numerical techniques of computing Bingham type fluid, the main difficulty is how to deal with the stress below the yield stress τ, as it is undetermined in the constitutive law. One way of addressing this problem is by considering the fluid as highly viscous when it is unyielded, thus making the strain rate close to 0. This is done by doing a regularization to the constitutive law as below:

$$\tau = \left(\mu + \frac{\tau_y}{\boldsymbol{\gamma} + \epsilon}\right)\gamma$$

where ϵ is a small parameter. If $\boldsymbol{\tau}$ is sufficiently bigger than τ_y, $\boldsymbol{\gamma} \ll \epsilon$, the original constitutive equation is recovered. A second way of addressing the undetermined stress field is by introducing a Lagrangian multiplier tensor λ, such that

$$\begin{cases} \boldsymbol{\gamma} = \lambda : \gamma \\ \tau = \mu\gamma + \tau_y\lambda \end{cases}$$

everywhere in the fluid. Theories prove the existence of such λ, including the region $\boldsymbol{\gamma} = 0$, so that the stress can be recovered everywhere. We

refer to Dean[6] for a review of those methods. However, since the original constitutive law does not give any information for the stress in the unyielded region, thus recovering of unyielded stress field in the numerical schemes is artificial.

Numerical simulations of gravity current of Bingham type fluid are rare. Vola et al[4] developed a numerical scheme of computing gravity currents of Non-Newtonian fluid, using a Lagrangian technique. Roussel and Coussot[19] used a software FLOW-3D to simulate the slump of a cylinder of Bingham fluid. Staron et al[15] did a simulation of columns of Bingham plastics under gravity, using regularization methods.

For experiments about this problem, there are no experimental results with the same context as ours now. Published papers with related experiments include Pashias et al[23] (measurement of the yield stress by the slump test), Cochard and Ancey[24] (experimental results related to the dam-break problem for viscoplastic fluids which is a 3D case), and Balmforth et al[18] (experimental analysis of the dam break of a viscoplastic fluid in a horizontal channel, with Herschel-Bulkley constitutive law).

1.3 Objectives

Three theoretical models are given from the past literature, predicting the final shape of the slump of Bingham fluid in terms of the yield stress and the initial aspect ratio. Currently there are not many experiments to verify those models. Therefore, my thesis aims to use numerical simulations to compare with the theoretical models, in order to find the final shapes of a 2D unit block of Bingham fluid under gravity. I am using a Complex fluid solver on the platform Pelicans[25], developed by IRSN, to simulate the evolution.

Chapter 2

Problem Description

2.1 Problem setting

We study the slumping of a unit block of Bingham fluid under gravity, in a 2D case. We will consider a two-phase flow in a rectangular domain.

Figure 2.1 illustrates the domain and initial condition. The domain is set to be $\Omega = [0, L] \times [0, H]$. There are two fluids in the domain. Fluid 1 is what we are interested in, with a higher density ρ_1 and viscosity μ_1, which we also refer to as the lower layer. Fluid 2 is an ambient fluid, with much lower density ρ_2 and viscosity μ_2. We refer to this fluid as the upper layer.

Since we want the lower layer to be a Bingham fluid, it is necessary to define the constitutive law, which is

$$\begin{cases} \gamma = 0 & \boldsymbol{\tau_1}(u) < \tau_y \\ \tau_1(u) = \left(\mu_1 + \dfrac{\tau_y}{\boldsymbol{\gamma}}\right)\gamma(u) & \boldsymbol{\tau_1}(u) > \tau_y \end{cases}$$

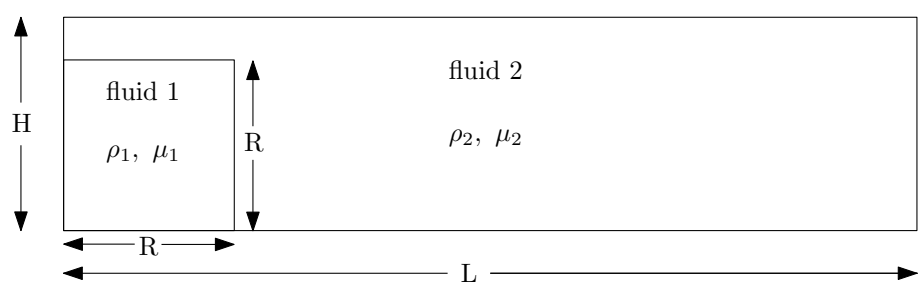

Figure 2.1: problem setting

And the upper layer is Newtonian, so that

$$\tau_2(u) = \mu_2 \gamma(u)$$

where $\tau_1(u), \tau_2(u)$ are the stress tensor, $\gamma(u) = \nabla u + (\nabla u)^T$ is the strain rate tensor, and $\boldsymbol{\tau_1}(u), \boldsymbol{\gamma}$ are the second invariants of $\tau_1(u), \gamma(u)$, respectively:

$$\boldsymbol{\tau_1}(u) = \sqrt{\frac{1}{2}\tau_1(u) : \tau_1(u)},\ \boldsymbol{\gamma}(u) = \sqrt{\frac{1}{2}\gamma(u) : \gamma(u)}$$

τ_y is the yield stress of fluid 1. That is, when the stress invariant exceeds τ_y, the flow will behave like fluid, otherwise it is like solid, with no local deformation.

2.2 Equations

Suppose both fluids are incompressible, the equations are defined as in equation (2.1),

$$\begin{aligned} \text{lower layer} &\begin{cases} \rho_1 \left[\dfrac{\partial u}{\partial t} + (u \cdot \nabla) u\right] = -\nabla p + \nabla \cdot \tau_1(u) + \rho_1 g \\ \nabla \cdot u = 0 \end{cases} \\ \text{upper layer} &\begin{cases} \rho_2 \left[\dfrac{\partial u}{\partial t} + (u \cdot \nabla) u\right] = -\nabla p + \nabla \cdot \tau_2(u) + \rho_2 g \\ \nabla \cdot u = 0 \end{cases} \end{aligned} \tag{2.1}$$

where $u = (v, w)$ is the velocity vector, p is the pressure, and g is the gravity. A no-slip boundary condition is applied on the bottom and top, where $u = (0, 0)$. A symmetry boundary condition is set on the left and right wall, where $v = 0, \frac{\partial w}{\partial x} = 0$. The velocity and stress must also be continuous at the interface.

2.3 Dimensionless form

Suppose the characteristic length and velocity are R and U, let $x = R\hat{x}, z = R\hat{z}, u = U\hat{u}, t = \frac{R}{U}\hat{t}$, where $U = \frac{\rho_1 g R^2}{\mu_1}$. Here, $\hat{u}, \hat{t}, \hat{p}, \hat{\tau}$ all stand for the dimensionless form. The equations are reduced to

$$\begin{aligned} &\text{lower layer} \begin{cases} Re\left[\dfrac{\partial \hat{u}}{\partial \hat{t}} + (\hat{u}\cdot\nabla)\hat{u}\right] = -\nabla\hat{p} + \nabla\cdot\hat{\tau}_1(\hat{u}) + \bar{1} \\ \nabla\cdot\hat{u} = 0 \end{cases} \\ &\text{upper layer} \begin{cases} \dfrac{\rho_2}{\rho_1} Re\left[\dfrac{\partial \hat{u}}{\partial \hat{t}} + (\hat{u}\cdot\nabla)\hat{u}\right] = -\nabla\hat{p} + \dfrac{\mu_2}{\mu_1}\nabla\cdot\hat{\tau}_2(\hat{u}) + \dfrac{\rho_2}{\rho_1}\bar{1} \\ \nabla\cdot\hat{u} = 0 \end{cases} \end{aligned} \tag{2.2}$$

and the constitutive law is reduced to

$$\begin{cases} \hat{\tau}_1(\hat{u}) = \left(1 + \dfrac{B}{\hat{\boldsymbol{\gamma}}}\right)\hat{\gamma} \\ \hat{\tau}_2(\hat{u}) = \hat{\gamma} \end{cases} \tag{2.3}$$

where $Re = \frac{\rho_1^2 g R^3}{\mu_1^2}$ is the Reynolds number, and $B = \frac{\tau_y}{\rho_1 g R}$ is the Bingham number, which is the dimensionless yield stress. For convenience, in the rest of this thesis, we just use u, p, τ, γ to represent the dimensionless form.

Chapter 3

Asymptotic Results

We will start by considering a Newtonian fluid for the lower layer, and then extend to a Bingham fluid.

3.1 A Newtonian two-layer model

A dimensionless model for the propagation of two-dimensional Newtonian film under gravity is discussed by Huppert[7].

$$\frac{\partial h}{\partial t} = \frac{1}{3}\frac{\partial}{\partial x}\left(h^3 \frac{\partial h}{\partial x}\right)$$

It is based on the assumption that there is only one layer of fluid and the shear stress on the surface is 0. In our problem, there is an ambient fluid above the lower layer. If both are Newtonian fluids, the Navier-Stokes equation is written as below.

$$\begin{aligned} &\text{lower layer} \begin{cases} u_x + w_z = 0 \\ \rho_1(u_t + uu_x + wu_z) = -p_x + \mu_1(u_{xx} + u_{zz}) \\ \rho_1(w_t + uw_x + ww_z) = -p_z + \mu_1(w_{xx} + w_{zz}) + \rho_1 g \end{cases} \\ &\text{upper layer} \begin{cases} u_x + w_z = 0 \\ \rho_2(u_t + uu_x + wu_z) = -p_x + \mu_2(u_{xx} + u_{zz}) \\ \rho_2(w_t + uw_x + ww_z) = -p_z + \mu_2(w_{xx} + w_{zz}) + \rho_2 g \end{cases} \end{aligned} \tag{3.1}$$

where (u, w) is the velocity vector. Now suppose the upper layer is not ignored, and the viscosity ratio and density ratio are $S = \frac{\mu_2}{\mu_1}, Q = \frac{\rho_2}{\rho_1}$. Using a similar non-dimensionalization methods as in [22], with different length

scale for the horizontal and vertical length, let

$$x = L\hat{x}, z = R\hat{z}, U = \frac{\rho_1 g R^3}{\mu_1 L}, v = (u, w) = \left(U\hat{u}, \frac{R}{L}U\hat{w}\right), t = \frac{L}{U}\hat{t}, p = \rho g R\hat{p}, \hat{H} = H/R$$

and suppose $\frac{R}{L} = \epsilon \ll 1, Re = \frac{\rho_1 U R^2}{\mu_1 L} \ll 1$. Equation (3.1) is nondimensionalized as

$$\text{lower layer} \begin{cases} u_x + w_z = 0 \\ Re(u_t + uu_x + wu_z) = -p_x + \epsilon^2 u_{xx} + u_{zz} \\ Re(w_t + uw_x + ww_z) = -\frac{1}{\epsilon^2}(p_z + 1) + \epsilon^2 w_{xx} + w_{zz} \end{cases}$$
$$\text{upper layer} \begin{cases} u_x + w_z = 0 \\ \frac{Q}{S}Re(u_t + uu_x + wu_z) = -\frac{1}{S}p_x + \epsilon^2 u_{xx} + u_{zz} \\ \frac{Q}{S}Re(w_t + uw_x + ww_z) = -\frac{1}{\epsilon^2 S}(p_z + Q) + \epsilon^2 w_{xx} + w_{zz} \end{cases} \tag{3.2}$$

Getting rid of $O(\epsilon)$ term, we have

$$\begin{cases} p_x = u_{zz}, \quad p_z = -1 & \text{for the lower layer} \\ p_x = Su_{zz}, \quad p_z = -Q & \text{for the upper layer} \end{cases} \tag{3.3}$$

Let $h = h(x, t)$ be the height of the lower layer. In order to solve equation 3.3, we need to include the following conditions.

- no-slip condition on the upper and lower boundary, $u = 0$ at $z = 0, 1$.
- u, p, τ continuous at the interface, here $\tau \approx \mu u_z$.
- zero flux across the domain, $\int_0^{\hat{H}} u dz = 0$.

Combining all the relations above, we obtain

$$\begin{cases} u = 0 & z = 0 \\ u_{zz} = p_x, p_z = -1 & 0 < z < h \\ u, p, \tau \text{ continuous} & z = h \\ Su_{zz} = p_x, p_z = -Q & h < z < \hat{H} \\ u = 0 & z = \hat{H} \\ \displaystyle\int_0^{\hat{H}} u dz = 0 & \\ \displaystyle h_t = \frac{\partial}{\partial x}\left(\int_0^h u dz\right) & \end{cases} \tag{3.4}$$

Then we derive a two-layer model for a shallow gravity flow.

$$\frac{\partial h}{\partial t} = \frac{1}{3}(1-Q)\frac{\partial}{\partial x}\left(\frac{(k+Sh)}{(k^2-Sh^2)^2+4Skh\hat{H}^2}h^3k^3\frac{\partial h}{\partial x}\right)$$

where $k = \hat{H} - h$. As $S \to 0$ and $Q \to 0$, the equation is reduced to Huppert's model. Notice that this model is only valid for large aspect ratio, where the horizontal length scale is much more than the vertical, so that τ can be approximated as μu_z. Therefore, it may not be valid at the flow front. This is to be shown in the next chapter, in comparison with numerical simulations.

3.2 A Bingham-Newtonian two-layer model

For shallow layer model for Bingham fluid, Liu and Mei[12] presented the lubrication model for two dimensional flow.

$$\frac{\partial h}{\partial t} = \frac{1}{6}\frac{\partial}{\partial x}\left(Y^2(3h-Y)\frac{\partial h}{\partial x}\right) \tag{3.5}$$

Y is the height of the yielded region, which satisfies

$$Y = \max\left\{h - \frac{B}{|h_x|}, 0\right\}$$

This model assumes that there is only one layer of Bingham fluid, and the shear stress on the surface is 0. Therefore, there is always an unyielded region on the top of the fluid.

Therefore we consider the problem with a Newtonian fluid above a Bingham fluid, so that the stress on the surface is balanced by the upper fluid, and give the following analysis. Using a similar nondimensionalization procedure as for the Newtonian two-layer model, we get the reduced form.

$$\begin{cases} p_x = \partial_z \tau, & p_z = -1, & 0 < z < h \\ p_x = S u_{zz}, & p_z = -Q, & h < z < \hat{H} \end{cases} \tag{3.6}$$

as in equation (3.3), the only difference is that u_{zz} is replaced by $\partial_z \tau$. Since p_z is piecewise linear, we can integrate to get

$$\begin{cases} p = P - (z - h), & \tau = \tau_0 + (P_x + h_x) z & 0 < z < h \\ p = P - Q(z - h), & p_x = S u_{zz} & h < z < \hat{H} \end{cases} \tag{3.7}$$

For the lower layer $0 < z < h$, define $\tau_0 = \tau(x, 0), \tau_h = \tau(x, h)$, equation (3.7) gives a relation

$$\tau_h = \tau_0 + (P_x + h_x) h$$

Let us define u_z as a function of τ, $u_z = \Gamma(\tau)$, using the constitutive law As τ is a linear function of z.

$$\frac{z}{h} = \frac{\tau - \tau_0}{\tau_h - \tau_0}$$

differentiating the equation above gives

$$dz = \frac{h}{\tau_h - \tau_0} d\tau$$

The velocity at the interface u_h is

$$u_h = \int_0^h u_z dz = \frac{h}{\tau_h - \tau_0} \int_{\tau_0}^{\tau_h} \Gamma(\tau) d\tau$$

For convenience, define $I_0 = \int_{\tau_0}^{\tau_h} \Gamma(\tau) d\tau$, so that

$$u_h = \frac{hI_0}{\tau_h - \tau_0}$$

And the flux of the lower layer is integrated as

$$\begin{aligned}\int_0^h u dz &= zu|_0^h - \int_0^h z u_z dz \\ &= hu_h - \int_{\tau_0}^{\tau_h} \frac{h(\tau - \tau_0)}{\tau_h - \tau_0} \Gamma(\tau) dz \frac{h}{\tau_h - \tau_0}\end{aligned}$$

If we define $I_1 = \int_{\tau_0}^{\tau_h} \tau \Gamma(\tau) d\tau$, we can rewrite the flux integral so that

$$\int_0^h u dz = \frac{h^2(\tau_h I_0 - I_1)}{(\tau_h - \tau_0)^2}$$

For the upper layer $h < z < \hat{H}$, since $P_x + Qh_x = Su_{zz}$ at and $Su_z|_h = \tau_h$, we have

$$u_z = \frac{1}{S} \left[(P_x + Qh_x)(z - h) + \tau_h \right]$$

Introducing $P_x = \frac{\tau_h - \tau_0}{h} - h_x$ furnishes

$$Su_z = \frac{1}{S} \left[\left(\frac{\tau_h - \tau_0}{h} - h_x + Qh_x \right) (z - h) + \tau_h \right]$$

We can get the interface velocity u_h again by integrating u_z in the upper layer

$$\begin{aligned}u_h &= -\int_h^{\hat{H}} u_z dz \\ &= -\frac{1}{S}(\hat{H} - h) \left[\tau_h + \frac{\hat{H} - h}{2} \left(\frac{\tau_h - \tau_0}{h} - h_x + Qh_x \right) \right]\end{aligned}$$

And the flux of the upper layer is

$$\begin{aligned}\int_h^{\hat{H}} u dz &= zu|_h^{\hat{H}} - \int_h^{\hat{H}} z u_z dz \\ &= -hu_h - \int_h^{\hat{H}} \frac{z}{S}\left[\tau_h + \left(\frac{\tau_h - \tau_0}{h} - h_x + Qh_x\right)(z-h)\right] dz \\ &= -\frac{1}{2S}(\hat{H}-h)^2\tau_h - \frac{1}{3S}(\hat{H}-h)^3\left(\frac{\tau_h-\tau_0}{h} - h_x + Qh_x\right)\end{aligned} \tag{3.8}$$

To make the velocity continuous at the interface, and make zero flux across the region $\int_0^h u dz + \int_h^{\hat{H}} u dz = 0$, we have

$$\begin{cases} S\dfrac{hI_0}{\tau_h - \tau_0} = -(\hat{H}-h)\left[\tau_h + \dfrac{\hat{H}-h}{2}\left(\dfrac{\tau_h-\tau_0}{h} - h_x + Qh_x\right)\right] \\ \dfrac{h^2(\tau_h I_0 - I_1)}{(\tau_h-\tau_0)^2} = \dfrac{1}{2S}(\hat{H}-h)^2\tau_h + \dfrac{1}{3S}(\hat{H}-h)^3\left(\dfrac{\tau_h-\tau_0}{h} - h_x + Qh_x\right)\end{cases} \tag{3.9}$$

The evolution equation $h_t + (\int_0^h u dz)_x = 0$, becomes

$$\frac{\partial h}{\partial t} + \frac{\partial}{\partial x}\left[\frac{h^2}{(\tau_h-\tau_0)^2}(\tau_h I_0 - I_1)\right] = 0$$

For Bingham fluid, the relation of u_z and τ is

$$u_z = \Gamma(\tau) = \begin{cases} \tau - B & |\tau| > B \\ 0 & |\tau| < B \end{cases}$$

Using equation (3.9), τ_h, τ_0 can be solved by a Newton iteration method in each time step, as indicated in [9]. If $S \to 0, Q \to 0$, the equation is reduced to equation (3.5).

This equation indicates a final state of the flow as

$$h(x) = \sqrt{2B(X-x)}$$

Where X is the flow length of the final shape. In our case, since the total volume is 1, we can calculate the value of X by demanding $\int_0^X h(x)dx = 1$

and get the final flow length and height as a function of B:

$$X = \frac{1}{2}\left(\frac{9}{B}\right)^{1/3}, H_0 = h(0) = (3B)^{1/3}$$

3.3 Final shape from plasticity theory

Dubash et al [20] provided a higher order solution to the steady state of the Bingham slump. For $B \ll 1$

$$h = \sqrt{\left(1+\frac{\pi}{2}B\right)^2\left(\frac{1}{3B}+\frac{\pi}{4}\right)^{-2/3} - 2Bx} - \frac{\pi}{2}B\left(\frac{1}{3B}+\frac{\pi}{4}\right)^{-1/3} + O(B^3)$$

This model assumes the flow height is normalized to be 1. In our settings, as the total volume is 1, the final height and length are

$$\begin{cases} H_0 = \left(\frac{1}{3B}+\frac{\pi}{4}\right)^{-1/3} \\ X = \left(\frac{1}{2B}+\frac{\pi}{2}\right)\left(\frac{1}{3B}+\frac{\pi}{4}\right)^{-2/3} \end{cases} \tag{3.10}$$

Figure 3.1 illustrates the final shape of the fluid for varying Bingham number, predicted by equation 3.10. Dubash [20] also used a slipline method of plasticity theory to compute the final shape, based on the assumption that the flow is yielded everywhere before reaching the steady state, so that stress falls to the yielded stress τ_y everywhere. There is no explicit form of the final shape in terms of B, algorithms about construction of the slipline field can be found in the reference. Figure 3.2 illustrates the final shape of the fluid for varying Bingham number, predicted by the slipline theory.

3.4 Relations of slump and aspect ratio

Other than shallow-layer analysis, Pashias et al[23] derived a relation of the slump height h and yield stress B, as well as the initial aspect ratio

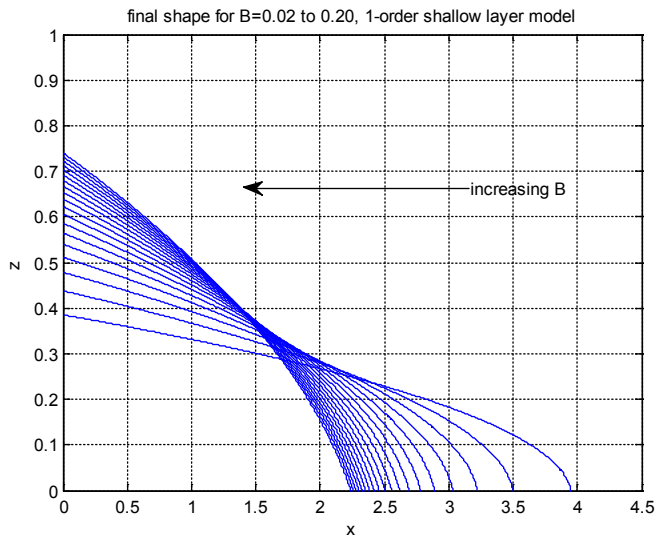

Figure 3.1: final shape for B=0.02 to 0.3 by 1-order shallow layer model

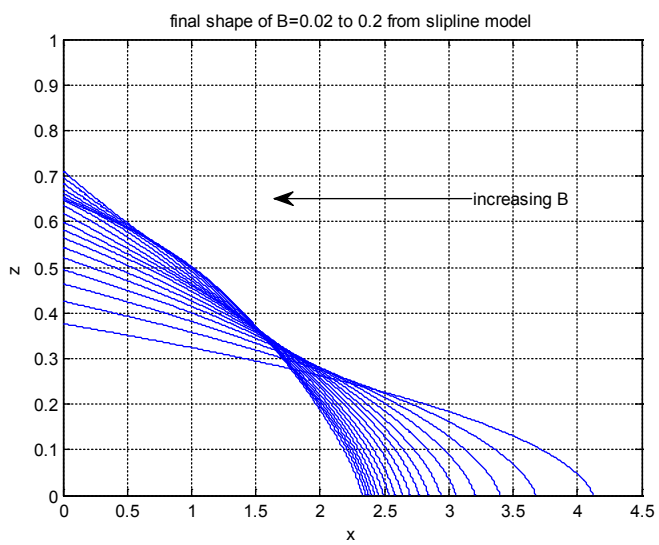

Figure 3.2: final shape for B=0.02 to 0.2 by slipline model

$H_0/R_0 = a$.

$$h = 1 - 2B[1 - \ln(2Ba)]$$

However this is based on the assumption that the aspect ratio is large and the stress variations in the horizontal direction are negligible compared to those in the vertical direction, which is different from our assumption. Nevertheless, it is still worth comparing with their model for relatively greater aspect ratio.

Staron et al[15] did numerical simulations in the same context as ours, except that the aspect ratio is varying from 0.2 to 19(in our problem it is kept unity). They get a relations of the slump height and the yield stress.

$$h = 3.01B^{0.66}$$

This relation is based on the observation of a group of numerical tests with varying B and initial aspect ratio.

Chapter 4

Numerical Results

4.1 Numerical scheme

We use a Volume-of-Fluid method to simulate the two-phase fluid. We refer to Hirt and Nichols[8] for a description of this method. In brief, a concentration field $c(x, y, t)$ is introduced to distinguish the two fluids and smooth out the interface between them: $c = 1$ for the lower layer, and $c = 0$ for the upper layer. This field is taken to be a material invariant. The problem therefore boils down to the Navier-Stokes equation and the advection-diffusion equation:

$$\begin{cases} Re(c)\left[\dfrac{\partial u}{\partial t} + (u \cdot \nabla)u\right] = -\nabla p + \nabla \cdot \tau(u) + Ri(c)g \\ \nabla \cdot u = 0 \\ \dfrac{\partial c}{\partial t} + \nabla \cdot (uc) = 0 \end{cases} \tag{4.1}$$

where

$$Re(c) := \left[c + (1-c)\frac{\rho_2}{\rho_1}\right]\frac{\rho_1 U R}{\mu_1}$$

$$Ri(c) := \left[c + (1-c)\frac{\rho_2}{\rho_1}\right]\frac{\rho_1 g R^2}{\mu_1 U}$$

$$\tau(u) := \left[c + (1-c)\frac{\mu_2}{\mu_1}\right]\gamma(u)$$

In every time step, the Navier-Stokes equation is solved using a Galerkin finite element method. And then the advection diffusion equation is solved using a finite volume method, with a MUSCL scheme in the advection term. We refer to Mikhlin [26] for a description of Galerkin method and Van

Leer[14] for a description of MUSCL scheme.

4.1.1 Regularization method for Navier-Stokes equations

For a general Navier-Stokes equation, with no-slip condition in Γ_D, no-flux condition in Γ_N, as below

$$\begin{cases} \rho\left(\dfrac{\partial u}{\partial t} + (u\cdot\nabla)u\right) = -\nabla p + \nabla\cdot\tau(u) + \rho g & in\ \Omega \\ \nabla\cdot u = 0 & in\ \Omega \\ u = 0 & in\ \Gamma_D \\ \nabla u\cdot n = 0 & in\ \Gamma_N \end{cases} \tag{4.2}$$

Here $\tau(u)$ is given by the regularized constitutive law.

$$\tau(u) = \left[c(1+\frac{B}{\gamma+\epsilon}) + (1-c)\frac{\mu_2}{\mu_1}\right]\gamma(u)$$

where ϵ is the regularization parameter. On a certain time t^n, given the current velocity field u^n, time step Δt, the discrete scheme for solving u^{n+1} is

$$\begin{cases} \dfrac{\rho}{\Delta t}u^{n+1} + (\rho u^n\cdot\nabla)u^{n+1} - \nabla\cdot\tau(u^{n+1}) + \nabla p^{n+1} = \rho g + \dfrac{\rho}{\Delta t}u^n & in\ \Omega \\ \nabla\cdot u^{n+1} = 0 & in\ \Omega \\ u^{n+1} = 0 & in\ \Gamma_D \\ \nabla u^{n+1}\cdot n = 0 & in\ \Gamma_N \end{cases} \tag{4.3}$$

The variational form is: Find $(u,p)\in S^u\times V^p$ so that for $\forall(v,q)\in V^u\times V^p$:

$$\begin{aligned} \frac{1}{\Delta t}\int_\Omega \rho u\cdot v + \int_\Omega(\rho u^n\cdot\nabla)u\cdot v + \int_\Omega \tau(u):\nabla v - \int_\Omega p\nabla\cdot v = \\ \int_\Omega \rho g\cdot v + \frac{1}{\Delta t}\int_\Omega \rho u^n\cdot v \\ \int_\Omega q\nabla\cdot u = 0 \end{aligned} \tag{4.4}$$

Here S^u, V^u, V^p is defined as

$$\begin{aligned} S^u &= \{v \in H^1(\Omega) | v = 0 \ in \ \Gamma_D\} \\ V^u &= \{v \in H^1(\Omega) | v = 0 \ in \ \Gamma_D\} \\ V^p &= L^2(\Omega) \end{aligned} \tag{4.5}$$

We can rewrite this in a simple way

$$\begin{aligned} \frac{1}{\Delta t} m(u,v) + c(u^n; u, v) + k(u,v) + b(v,p) &= f(v) \\ b(u,q) &= 0 \end{aligned} \tag{4.6}$$

where

$$\begin{aligned} m(u,v) &= \int_\Omega \rho u \cdot v \\ c(u; v, w) &= \int_\rho (u \cdot \nabla) v \cdot w \\ k(u,v) &= \int_\Omega \tau(u) : \nabla v \\ b(v,q) &= -\int_\Omega q \nabla \cdot v \\ f(v) &= \int_\Omega \rho g \cdot v - \frac{1}{\Delta t} m(u^n, v) \end{aligned} \tag{4.7}$$

This variational equation is then solved using a Galerkin method. On a finite dimensional subspace $V_n^u \subset V^u, V_h^p \subset V^p$

$$\begin{aligned} \frac{1}{\Delta t} m(u_h, v_h) + c(u_h^n; u_h, v_h) + k(u_h, v_h) + b(v_h, p_h) &= f(v_h) \\ b(u_h, q_h) &= 0 \end{aligned} \tag{4.8}$$

After a finite element basis is chosen,

$$X_h = span\{\psi_k^u \mid 0 \leq k < N_{dof}^u\}$$

$$M_h = span\{\psi_k^p \mid 0 \leq k < N_{dof}^p\}$$

the variational equation is transformed to the linear system,

$$\begin{cases} \dfrac{1}{\Delta t} MU + M_R U + AU + B^T P = F \\ \qquad\qquad\qquad\qquad\qquad\qquad BU = 0 \end{cases} \tag{4.9}$$

where

$$\begin{aligned} M_{IJ} &= m(\psi_J^u, \psi_I^u) && 0 \le I, J < N_{dof}^u \\ M_{RIJ} &= m_R(\psi_J^u, \psi_I^u) && (I, J) \in \Gamma_R \\ A_{IJ} &= c(u_h^n; \psi_J^u, \psi_I^u) + k(\psi_J^u, \psi_I^u) && 0 \le I, J < N_{dof}^u \\ B_{IJ} &= b(\psi_J^u, \psi_I^p) && 0 \le I < N_{dof}^p, 0 \le J < N_{dof}^u \\ F_I &= f(\psi_I^u) && 0 \le I, J < N_{dof}^u \end{aligned} \tag{4.10}$$

4.1.2 Augmented Lagrangian method for Navier-Stokes equations

Unlike the regularization method, the augmented Lagrangian method does not require the constitutive laws to be regularized, and can produce truly unyielded regions where $\boldsymbol{\gamma} = 0$. Given the Navier-Stokes equation

$$\begin{cases} \rho\left(\partial_t u + (u \cdot \nabla) u\right) = \nabla \cdot \tau + f & \in \Omega \\ \nabla \cdot u = 0 & \in \Omega \\ u = u_B(t) & on\ \Gamma \\ \tau = -pI + \sqrt{2} B \dfrac{D(u)}{|D(u)|} + 2\mu D(u) \end{cases}$$

where $D(u) = \frac{1}{2}\gamma = \frac{1}{2}[\nabla u + (\nabla u)^T]$, Duvaut and Lions derive the variational inequality model: Find $\{u(u), p(t)\} \in (H^1(\Omega))^d \times L^2(\Omega)$ such that

$$\begin{aligned}
\rho \int_\Omega \partial_t u(t) \cdot (v - u(t))dx + \rho \int_\Omega (u(t) \cdot \nabla) u(t) \cdot (v - u(t))dx \\
+\mu \int_\Omega \nabla u(t) : \nabla (v - u(t))dx + \sqrt{2}B(j(v) - j(u(t))) \\
- \int_\Omega p(t) \nabla \cdot (v - u(t))dx \geq \int_\Omega f(t) \cdot (v - u(t))dx, \quad \forall v \in V_B(t) \\
\nabla \cdot u(t) = 0 \quad in\ \Omega \\
j(v) = \int_\Omega |D(v)|dx, \quad \forall v \in (H^1(\Omega))^d \\
V_B(t) = \{v | v \in (H^1(\Omega))^d, v = u_B(t)\ on\ \Gamma\}
\end{aligned}$$

We refer to Dean [6] for a review of the algorithm. In our numerical simulation with this method, the convergence rate for the linear system solution is too slow for an adequate spacial resolution, thus we fail to get the numerical results with large deformation. Nevertheless, for larger Bingham number where there is little deformation, numerical results are achieved.

4.1.3 Algorithm for advection-diffusion equation

For any region Ω in the domain

$$\frac{\partial C}{\partial t} + \nabla \cdot (uC) = 0$$

can be integrated as

$$\frac{\partial}{\partial t} \int_\Omega C dx + \int_{\partial\Omega} C(u \cdot n) ds = 0$$

Suppose the region is chosen to be a rectangular mesh cell, with 4 sides. Then the equation on this cell can be discretized as

$$\frac{A}{\Delta t} C^{n+1} + \sum_{i \in \{n,e,s,w\}} L_i (u_i \cdot n_i) C_i^{n+1} = \frac{A}{\Delta t} C^n$$

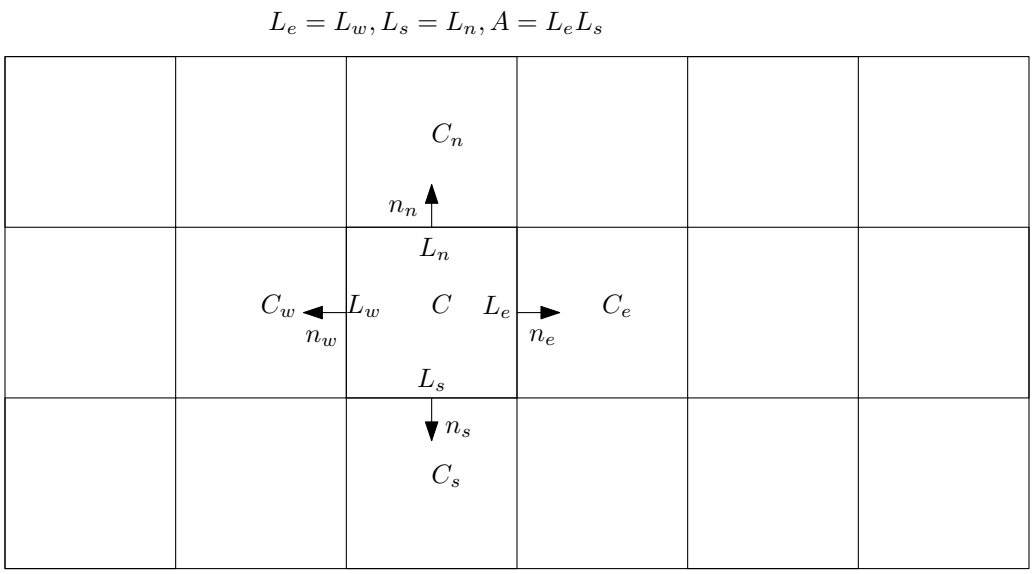

Figure 4.1: upwind scheme

where u_i is the approximated velocity at the middle point of side i, with outward normal n_i and length L_i, and C_i is C if $u_i \cdot n_i > 0$, or the adjacent cell of C with common side i if $u_i \cdot n_i < 0$. This is known as the upwind scheme. A is the cell area. The details are shown in Figure 4.1. This is the basic first order upwind scheme. The MUSCL scheme includes a second order correction term on the RHS, using a Van Leer limiter [14]:

$$\phi(r) = \frac{r + |r|}{1 + |r|}$$

which achieves more accurate solutions for large gradients in C, as is the case in our problem. In order to understand the use of the flux limiter, we refer to Kuzmin[13]. Figure 4.2 illustrates how this correction is computed, suppose $u \cdot n > 0$, then the correction term is computed as

$$\text{correction} = -ud \cdot L(u \cdot n)\phi\left(\frac{crg}{lhg}\right) lhg$$

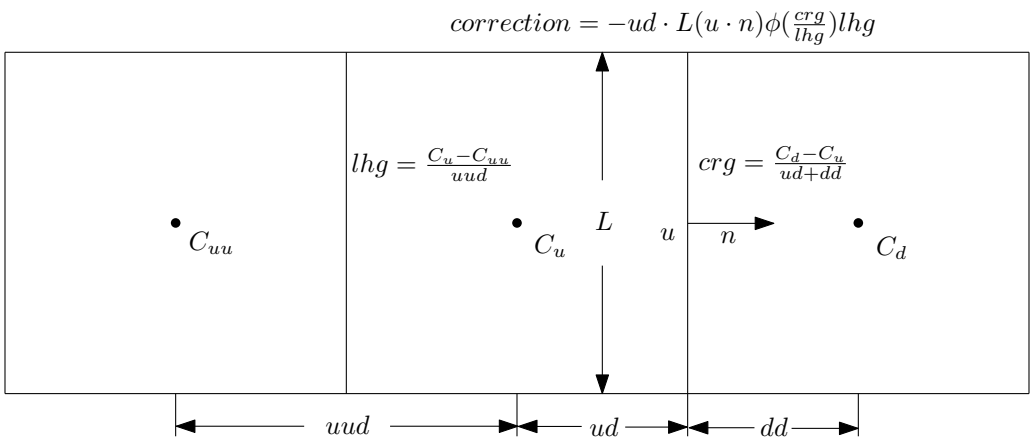

Figure 4.2: MUSCL scheme

It is added to the RHS of the equation for C_u, and its opposite value is added to the RHS of the equation for C_d. This scheme is implemented both on horizontal and vertical sides.

All of the algorithms above are implemented in C++ as an application of PELICANS, an object oriented platform developed at IRSN, France, to provide general frameworks and software components for the implementation of PDE solvers. PELICANS is distributed under the CeCILL license agreement. We refer to Hormozi[25] and Wielage-Burchard[11] for a detailed description of this code. [1]

4.2 Parameter settings

The domain size is chosen to be $[0, L] \times [0, H] = [0, 5] \times [0, 1.25]$, and the lower layer is initialized to be $[0, 1] \times [0, 1]$ on the left wall. The viscosity and density are normalized to be 1 for the lower layer , and 10^{-3} for the upper layer, so as to minimize the effect of the upper layer. The Reynolds number is set to be 9.81×10^{-4}, in order to minimize the effect of inertia force. We choose a uniform mesh on the domain, with $\Delta x = \Delta y$ varying from

[1] PELICANS is distributed under the CeCILL license agreement (http://www.cecill.info/licences/Licence CeCILL V2-en.html). PELICANS can be downloaded from https://gforge.irsn.fr/gf/project/pelicans/ .

0.005 to 0.025. For the computational reason, the maximum number of grid points we can achieve is $1000 \times 250 = 250000$. The time step for solving the Navier-Stokes equation is set to be $\Delta t = 0.5$, and the time step for solving the advection-diffusion equation is restricted by the CFL condition

$$\left(\frac{u}{\Delta x} + \frac{w}{\Delta y}\right) dt < \frac{1}{2}$$

where (u, w) is the velocity vector. The choice of all parameters are discussed in Appendix A.

4.3 Numerical result for Newtonian fluid problem

Before solving the Bingham fluid problem, it is necessary to test for a Newtonian problem to see if the code works well.

This problem is solved using the shallow layer model, and by numerical simulation. The results are compared below. Figure 4.3 is the flow profile at different time steps, the white curve is interface produced by the two-layer model. Figure 4.4 and 4.5 show the flow length and height as a function of time for different resolutions and the asymptotic model(Notice that as viscosity and density ratio are close to 0, the two-layer model is very close to the Huppert's model). According to the graph, the flow height is independent of resolution, while the flow length is converging slowly. Figure 4.6 illustrates a snapshot of the concentration field at time step $T = 250$. The white curve shows the interface, which is defined to be the level curve of $c = 0.5$. According to the graph, there is a 'finger' of upper fluid along the bottom underneath the lower fluid. Figure 4.7 shows the details of the finger, which is evidently poorly resolved. As a consequence of this resolution problem, the horizontal velocity from the bottom to the first layer of grid shows clear discontinuity, see Figure 4.8 for an example. In this graph, x-axis is the vertical position of the domain, and the y-axis is the horizontal velocity, plotted at $x = 3.5, T = 250$.

We attempted to resolve the finger by refining the resolution. However, even in our most refined resolution where the grid size is $\Delta y = 0.001$, the

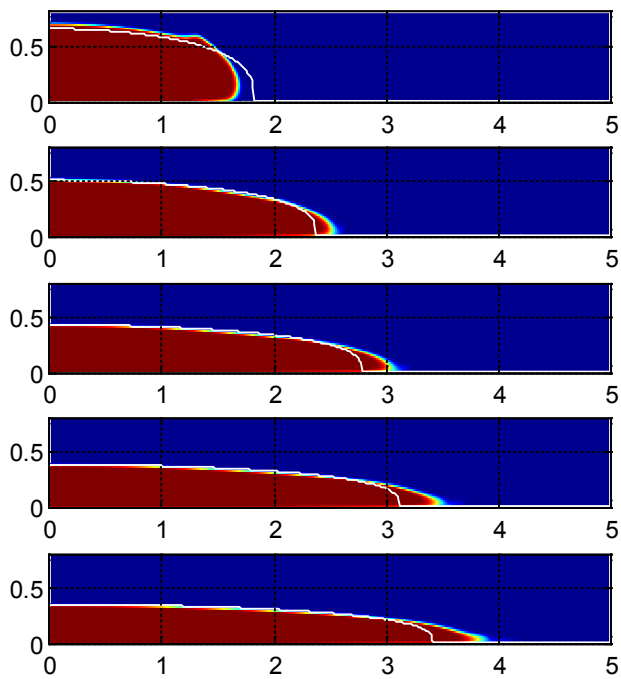

Figure 4.3: flow profile for $T = 10, 40, 90, 160, 250$, $\frac{\mu_2}{\mu_1} = \frac{\rho_2}{\rho_1} = 10^{-3}$, $Re = 9.81 \times 10^{-4}$

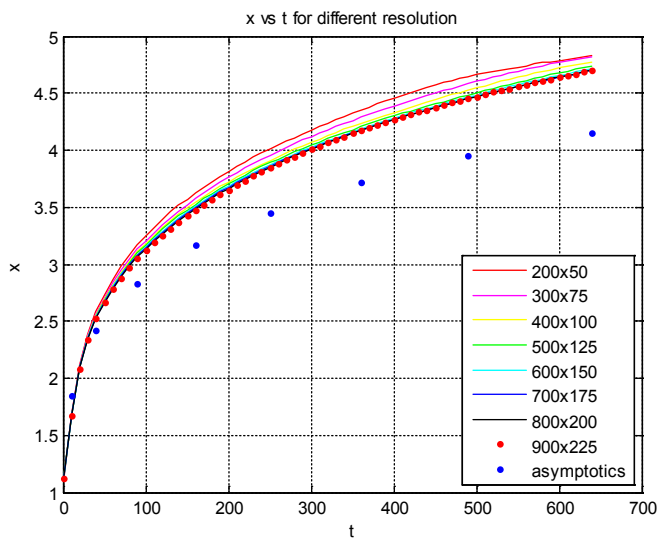

Figure 4.4: x vs t for different resolution, $\frac{\mu_2}{\mu_1} = \frac{\rho_2}{\rho_1} = 10^{-3},\ Re = 9.81 \times 10^{-4}$

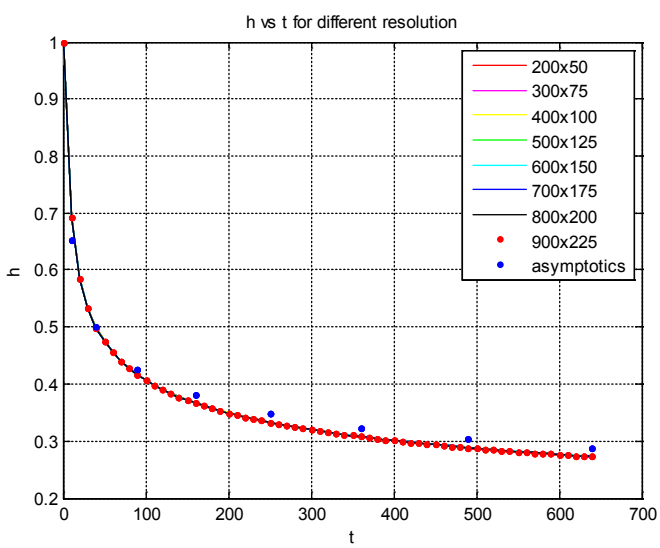

Figure 4.5: h vs t for different resolution, $\frac{\mu_2}{\mu_1} = \frac{\rho_2}{\rho_1} = 10^{-3},\ Re = 9.81 \times 10^{-4}$

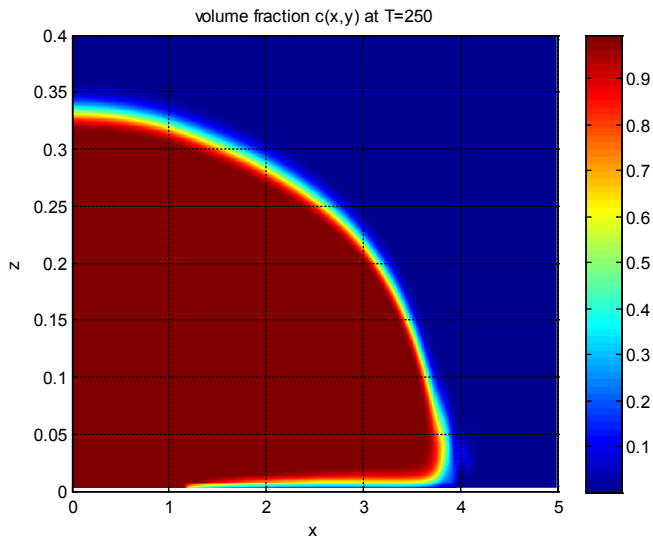

Figure 4.6: concentration profile at $T = 250$, $\frac{\mu_2}{\mu_1} = \frac{\rho_2}{\rho_1} = 10^{-3}$, $Re = 9.81 \times 10^{-4}$

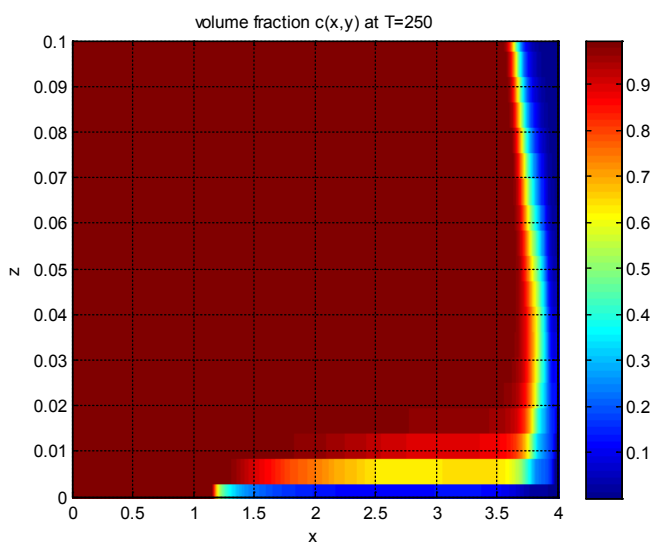

Figure 4.7: details about the concentration layer on the bottom

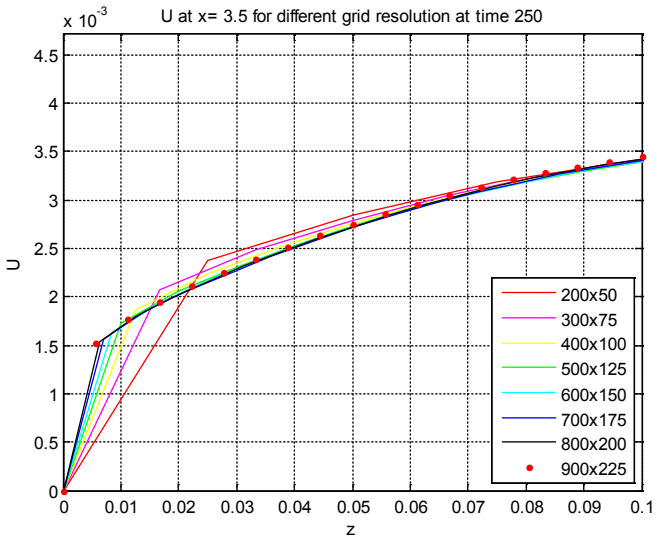

Figure 4.8: horizontal velocity at $x = 3.5,\ T = 250$, there is evident discontinuity in velocity field

'finger' is still there and velocity is still effectively discontinuous. Figure 4.9 shows a plot of the numerical scheme. To make the shear stress $\mu\frac{\partial u}{\partial z}$ continuous around the boundary, we have

$$\left[c_1 + (1-c_1)10^{-3}\right]\frac{u_2 - u_1}{\Delta y} \approx \left[c_0 + (1-c_0)10^{-3}\right]\frac{u_1 - u_0}{\Delta y}$$

Getting rid of all small terms, and notice that the finger on the bottom implies $c_0 \approx 0.1, c_1 \approx 1$, we will have

$$\frac{u_2 - u_1}{u_1 - u_0} = \frac{u_2 - u_1}{\Delta y} \times \left(\frac{u_1 - u_0}{\Delta y}\right)^{-1} \approx \frac{c_0}{c_1} \approx 0.1$$

This difference in velocity gradient explains why velocity field is not resolved.

4.4 The no-slip boundary condition

The finger is believed to be a direct result of imposing a no-slip boundary condition. Since the boundary velocity is 0, the fluid near the bottom sticks

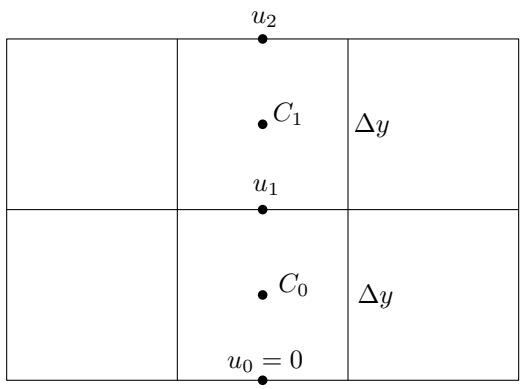

Figure 4.9: numerical scheme around the boundary, stress in the grid cell is interpolated by velocity at the vertex

to it. This is a common problem in dealing with the moving contact line. The same finger problem can be found in Hartel et al[2]. We may have a look at another case about the finger, which leads to more severe problem. Suppose the viscosity ratio $\frac{\mu_2}{\mu_1}$ and density ratio $\frac{\rho_2}{\rho_1}$ are all reset to be 0.1, which means the upper layer is heavier and more viscous than before, then there is an obvious finger on the bottom. See Figure 4.10, the flow profile for different time steps for this case.

In this case, a layer of the lighter fluid is underneath the heavier one. We do not know if this makes sense physically, as there are no related experiments. According to our analysis, if the finger is physically true, then the only way to resolve it is to refine the resolution along the bottom. However, due to our computation ability, we are not able to resolve the finger. If the finger is a numerical artefact, then we should think of ways to remove it, so that there is no resolution issue caused by the finger. In this situation, we can only deal with the case that the finger is not physically true, and we choose to remove the finger by introducing a slip condition on the bottom. From a physical viewpoint, there are several studies showing that there exists slip at some micro-scale surface, see Chang-Hwan Choi et al[3] for example. The slip length is of a μm scale, which is far from the macroscopic description of our problem. The slip condition we are trying to implement

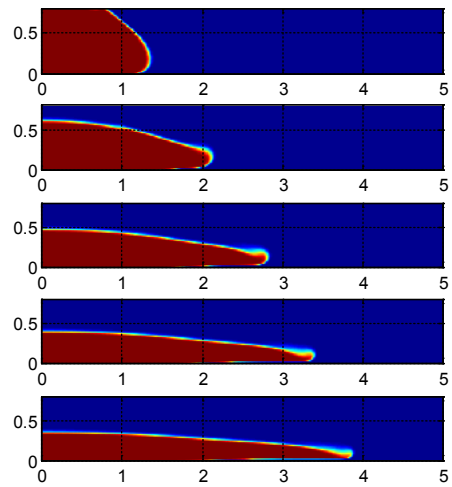

Figure 4.10: no-slip condition problem, $T = 10, 40, 90, 160, 250$, $\frac{\mu_2}{\mu_1} = \frac{\rho_2}{\rho_1} = 10^{-1}$, $Re = 9.81 \times 10^{-4}$

is based on a numerical artefact, not physical reason. This is commonly used in removing the singularity in force. Liu et al[10], for example, solves for the spreading of droplet with a slip boundary condition. We also refer to Renardy et al[17] for a discussion about the slip boundary condition in VOF methods. As there is slip velocity along the bottom, the finger can be removed as the flux at the boundary is evidently increased. We first apply

$$u = \lambda \frac{\partial u}{\partial y}$$

which is known as the Navier slip condition. λ is usually chosen to be on the order of the mesh size Δy. So we choose $\lambda = \Delta y$, and solve for the problem with $\frac{\mu_2}{\mu_1} = \frac{\rho_2}{\rho_1} = 0.1$. Figure 4.11 is the flow profile at $T = 10, 40, 90, 160, 250$. Compared with the no-slip condition result 4.10, the finger is partly removed and the flow profile totally changes, which we think is reasonable, based on the assumption that the finger is numerical artefact. We also modified the

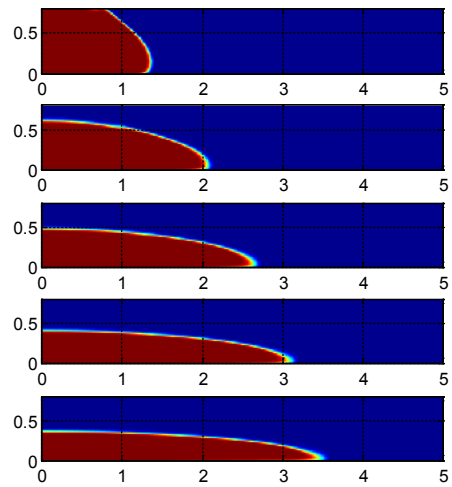

Figure 4.11: Navier slip boundary condition, $T = 10, 40, 90, 160, 250$, $\frac{\mu_2}{\mu_1} = \frac{\rho_2}{\rho_1} = 10^{-1}$, $Re = 9.81 \times 10^{-4}$

Navier slip condition to provide another model:

$$u = \frac{1-c}{c} \Delta y \frac{\partial u}{\partial y}$$

where $c = c(x, y)$ is the volume fraction, this is because the Navier slip condition does not fully remove the finger and there is still discontinuity in velocity field, see Figure 4.12, for example. And we add a term $\frac{1-c}{c}$, considering that, for $c = 1$ we have $u = 0$, meaning that the lower layer satisfies the no-slip condition, and for $c = 0$ we have $\frac{\partial u}{\partial y} = 0$, meaning that the upper layer satisfies the free slip condition, while for $0 < c < 1$ the two conditions are mixed. In this way, the finger is effectively removed, see Figure 4.13 and 4.14 for example, in those graphs the flow profile at the same time step for three different boundary conditions are compared, among which the finger is removed mostly by the modified slip model. Furthermore, the velocity field is continuous for the slip model, see Figure 4.15 as an example. Therefore, we choose the modified slip model

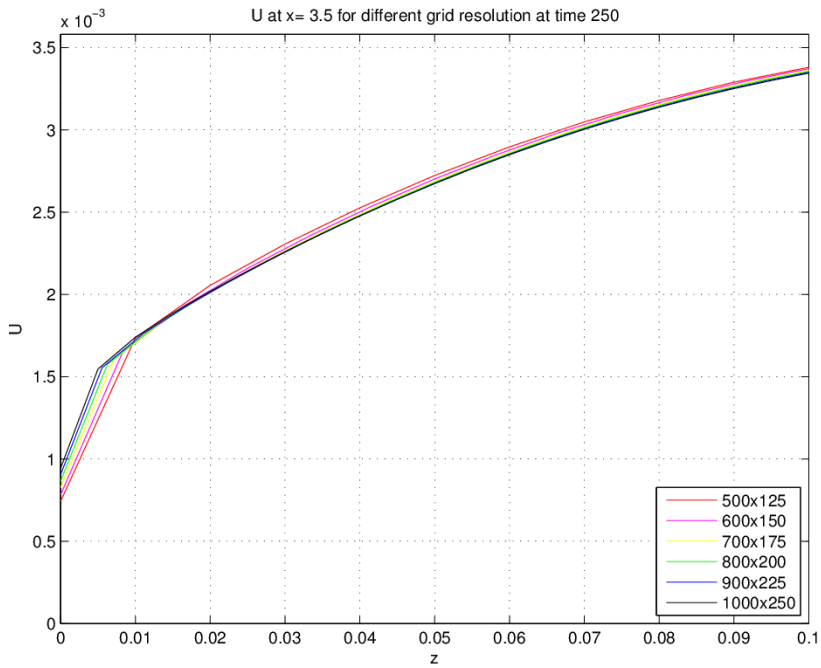

Figure 4.12: horizontal velocity at x=3.5, from Navier slip condition

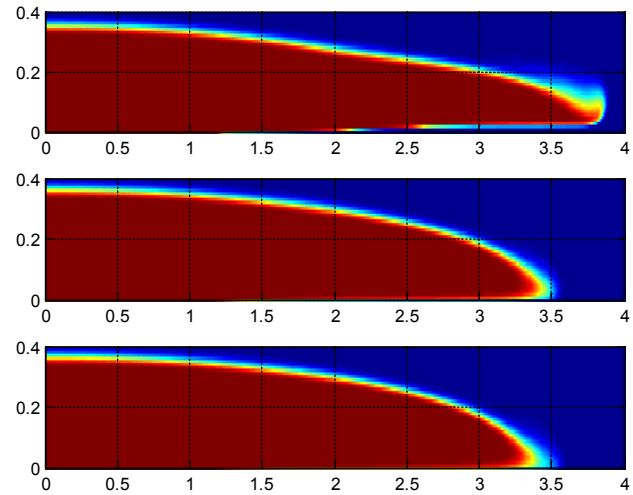

Figure 4.13: flow profile comparison of no-slip condition, Navier slip condition, modified slip condition, at the same time step, $T = 250$, $\frac{\mu_2}{\mu_1} = \frac{\rho_2}{\rho_1} = 10^{-1}$, $Re = 9.81 \times 10^{-4}$

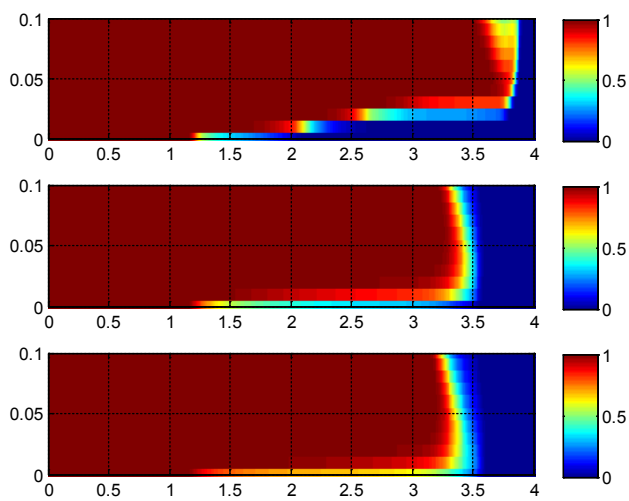

Figure 4.14: details about the finger, $T = 250$, $\frac{\mu_2}{\mu_1} = \frac{\rho_2}{\rho_1} = 10^{-1}$, $Re = 9.81 \times 10^{-4}$

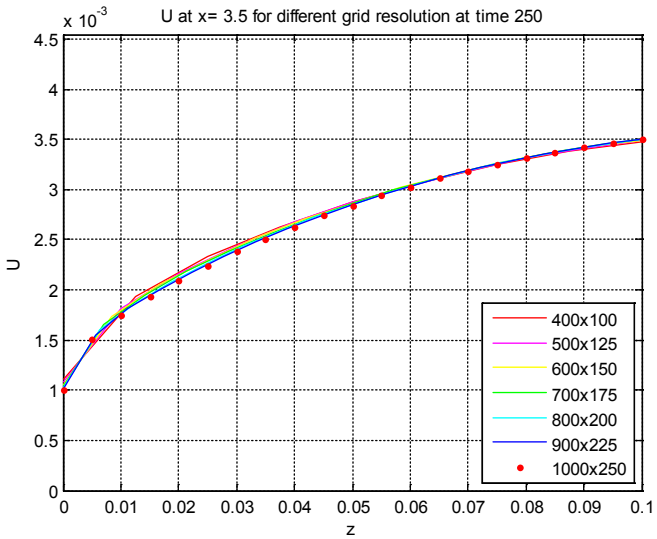

Figure 4.15: horizontal velocity at x=3.5, from modified slip condition, the velocity is continuous and converges well

$$u = \frac{1-c}{c}\Delta y \frac{\partial u}{\partial y}$$

as an alternate for the no-slip condition, in order to remove the finger and avoid the resolution issue. Figure 4.17 and 4.16 show better convergence of flow height and length versus time, than the no-slip condition. Thus we can assume that this model is independent of resolution, even though the boundary condition depends on the mesh size and the boundary volume fraction. Then we compare the numerical results with the asymptotic models, Figure 4.18 and 4.19 give the flow length and height vs time in the case $\frac{\mu_2}{\mu_1} = \frac{\rho_2}{\rho_1} = 0.1$. In principle, it is not reasonable to compare a numerical simulation with slip condition, with an asymptotic model, with no-slip condition. However, as the slip model depends on the mesh size, we cannot impose it into asymptotic analysis which does nothing about mesh. However, we want to argue that the slip model effectively reduces the propagation speed from the no-slip condition. That is, with a slip condition, the flow is expected to spread faster than no-slip condition, however, it is the

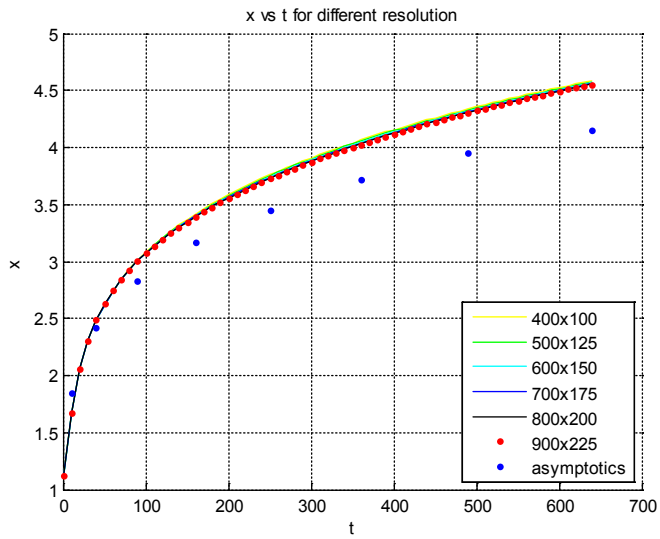

Figure 4.16: x vs t for modified slip model, $\frac{\mu_2}{\mu_1} = \frac{\rho_2}{\rho_1} = 10^{-1}$, $Re = 9.81 \times 10^{-4}$

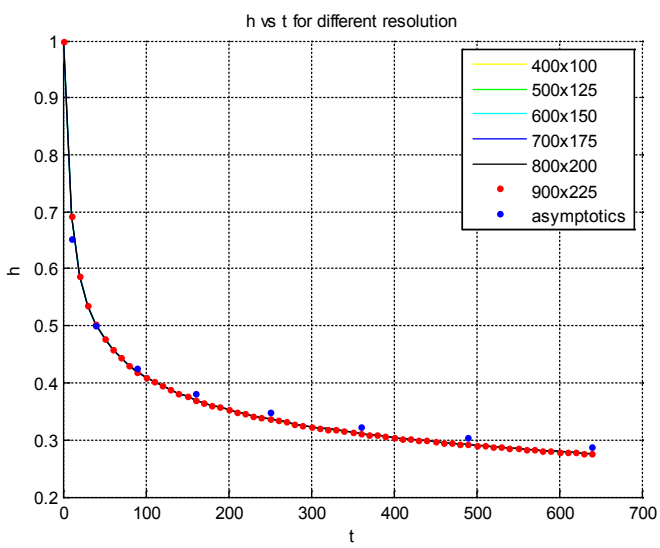

Figure 4.17: h vs t for modified slip model, $\frac{\mu_2}{\mu_1} = \frac{\rho_2}{\rho_1} = 10^{-1}$, $Re = 9.81 \times 10^{-4}$

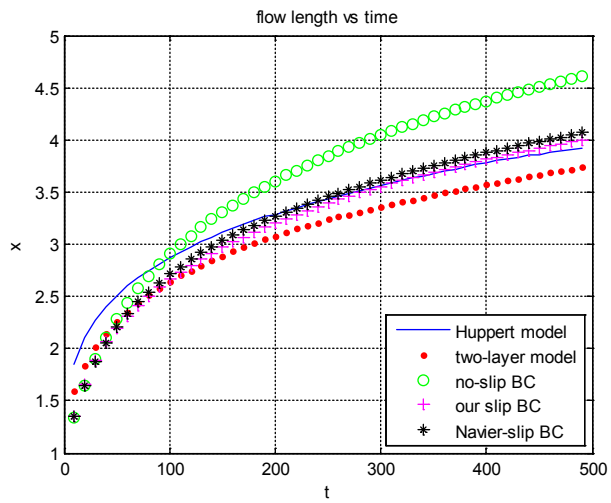

Figure 4.18: flow length vs time for different models, $\frac{\mu_2}{\mu_1} = \frac{\rho_2}{\rho_1} = 10^{-1}$, $Re = 9.81 \times 10^{-4}$

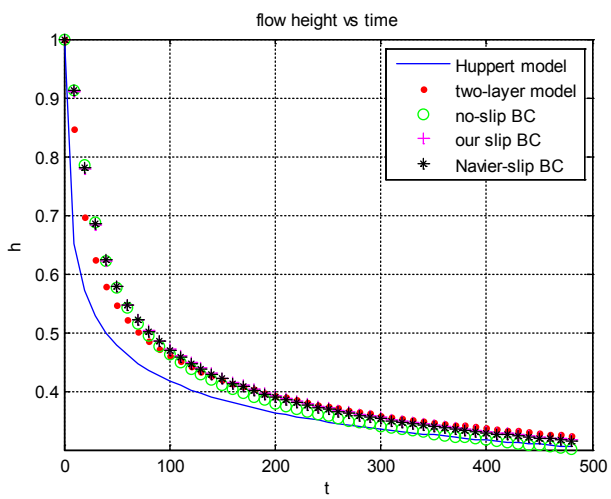

Figure 4.19: flow height vs time for different models, $\frac{\mu_2}{\mu_1} = \frac{\rho_2}{\rho_1} = 10^{-1}$, $Re = 9.81 \times 10^{-4}$

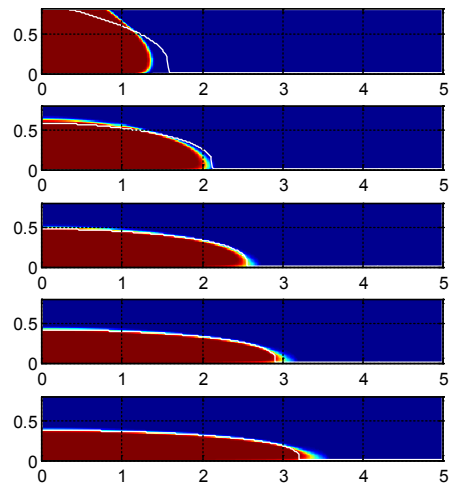

Figure 4.20: modified slip boundary condition, $T = 10, 40, 90, 160, 250$, $\frac{\mu_2}{\mu_1} = \frac{\rho_2}{\rho_1} = 10^{-1}$, $Re = 9.81 \times 10^{-4}$, white curves are from the two-layer shallow layer model

opposite. This might indicate that: in numerical simulation, imposing a slip condition might be more effective than a no-slip condition, in solving for a moving contact line problem. Figure 4.20 is the flow profile for different time steps, from the modified slip model, compared with the two-layer shallow layer theory. If the shallow layer theory is correct, that implies that the numerical results with a slip condition is similar to the asymptotic model with no-slip condition. In this case, we can think of the slip condition as a numerical artefact, aimed at recovering the resolution issue caused by the no-slip condition.

4.5 Discussion about the result

In our numerical simulation, we first impose a no-slip boundary condition on the bottom of the domain. However, the computation is not resolved, due to the existence of a finger of the upper fluid along the bottom. It is possible

that a highly refined resolution may help resolve the finger, however, our most refined resolution does not give a well-resolved result. Therefore, we change the boundary condition to be slip, in order to remove the finger. In our modified slip model $u = \frac{1-c}{c}\Delta y \frac{\partial u}{\partial y}$, it is still a no-slip condition as $c = 1$, but a free-slip condition as $c = 0$. This implies that for the lower layer, the boundary condition is still no-slip, but for the upper layer, the boundary condition is free-slip. Since we are not interested in the dynamics of the upper layer, imposing a free-slip condition will not cause severe problem. Then we make a resolution study of the modified slip model, the result is encouraging, because the finger is removed, and the velocity field near the boundary is resolved. Moreover, for the same problem considered, the slip model spreads more slowly than the no-slip model, meaning that numerically, the slip model is better to simulate the problem than the no-slip model. All these results are based on the assumption that the finger is a numerical effect. However, if the finger exists in reality, we have to have much refined resolution to resolve it. Also it is possible that the thickness of the finger is so small that its nature is beyond the reach of macro-scale fluid dynamics. Anyway, as the modified slip model is the best one so far in simulating our problem, we will impose it in the problem for Bingham fluid case.

4.6 Numerical result for Bingham fluid problem

Unlike Newtonian fluid, Bingham fluid will stop at a final state. In the previous chapter, we gave several theoretical models predicting the length and height of the final state, as well as the equilibrium flow profile. Now we will use numerical simulation to get the final shape, for varying yield stress. The numerical settings for the standard problem are

$$\frac{\rho_2}{\rho_1} = 10^{-3}, \frac{\mu_2}{\mu_1} = 10^{-3}, Re = 9.81 \times 10^{-4}$$

for varying Bingham number B from 0.02 to 0.6. The resolution is set to $\Delta x = \Delta y = 0.005$. Numerically, the regularized model $\tau = (1 + \frac{B}{\gamma + \epsilon})\gamma$ assumes that the viscosity is $O(\frac{B}{\epsilon})$ for small value of γ, thus the fluid will

never stop spreading. Therefore, it is necessary to define a stopping criteria. Remember in the numerical scheme, the constitutive law is

$$\tau(u) = \left[c\left(1 + \frac{B}{\boldsymbol{\gamma} + \epsilon}\right) + (1-c)\frac{\mu_2}{\mu_1}\right]\gamma(u)$$

Getting rid of small terms when $\epsilon \ll \boldsymbol{\gamma} \ll 1$, and take the second invariant, the fluid reaches the equilibrium as $\boldsymbol{\tau} \approx Bc$. Therefore in our problem the computation is considered as stopped when $\boldsymbol{\tau} < 1.01Bc$ everywhere in the fluid.

Figure 4.21 is the numerical final shape for B varying from 0.02 to 0.3, with slip and no-slip condition. For larger B, the fluid is unyielded from the very beginning, as the stress everywhere is below the yield stress. As $B < 0.28$, the fluid starts to spread, with a horn-like unyielded region on the upper right corner, which is not predicted by any asymptotic theories. And as B goes even lower, the unyielded region is less evident and flattened, and the flow is yielded everywhere, and it approaches certain final shape. The results of the no-slip condition has a finger on the bottom, the fluid spreads farther than the slip condition.

We will compare the numerical results with the following models from past literature:

- The 0-order shallow layer model

$$X = \frac{1}{2}\left(\frac{9}{B}\right)^{1/3}, \ H = (3B)^{1/3}$$

  This assumes that $B \ll 1$ so that the aspect ratio of the fluid is small.

- The 1-order shallow layer model

$$X = \left(\frac{1}{2B} + \frac{\pi}{2}\right)\left(\frac{1}{3B} + \frac{\pi}{4}\right)^{-2/3}, \ H = \left(\frac{1}{3B} + \frac{\pi}{4}\right)^{-1/3}$$

  from Dubash et al[20]. This again assumes $B \ll 1$.

- slipline theory model from Dubash et al[20], there is no explicit form of

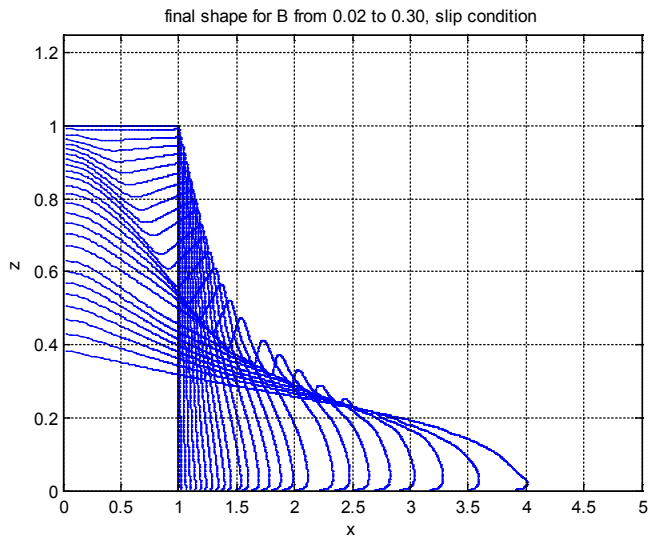

(a) slip condition

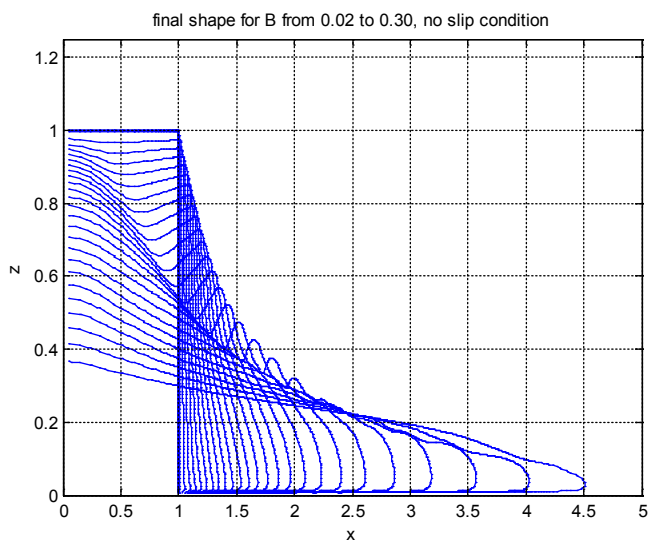

(b) no slip condition

Figure 4.21: final shapes for different B

the equation for the interface, the algorithm of recovering the interface is in this paper. It does not require B to be small, but assume the fluid yields everywhere at the beginning.

- Pashias et al[23] gives a relation of the equilibrium flow height and Bingham number
$$H = 1 - 2B[(1 - \ln(2B)]$$
It is based on the assumption of a much larger aspect ratio, while in our problem it is normalized to be 1. We include their result just to see how different the results are under different assumptions.

- Staron et al[15] gives a relation of the equilibrium flow height and Bingham number
$$H = 3.01B^{0.66}$$
They have generalized the relations of the equilibrium length and the Bingham number, but it is also dependent on viscosity in that model. As our methods of nondimensionalization are different, we do not have the viscosity available to compare, thus we only use the equilibrium height model.

For B in [0.02 0.1], the equilibrium spreading length and height are shown in Figure 4.22 and 4.23. Here we also include the numerical results with the no-slip condition to see the problem caused by the finger. In 4.22, the numerical no-slip results are still not resolved, leading to a further propagation than the numerical slip results and other theoretical models, for $B < 0.05$. Thus the numerical no-slip results are not believable, and the slip model makes the computation resolved, and it fits better with the asymptotic models than the no-slip results. As is said before, the modified slip model is the best one so far in simulating our problem, this comparison further confirms our expectation about the application of the slip model.
We can also see from the graphs that the numerical results agree well with 1-order shallow layer theory and the slipline theory for smaller B, this indicates that the shallow layer model and the slipline model from Dubash [20]

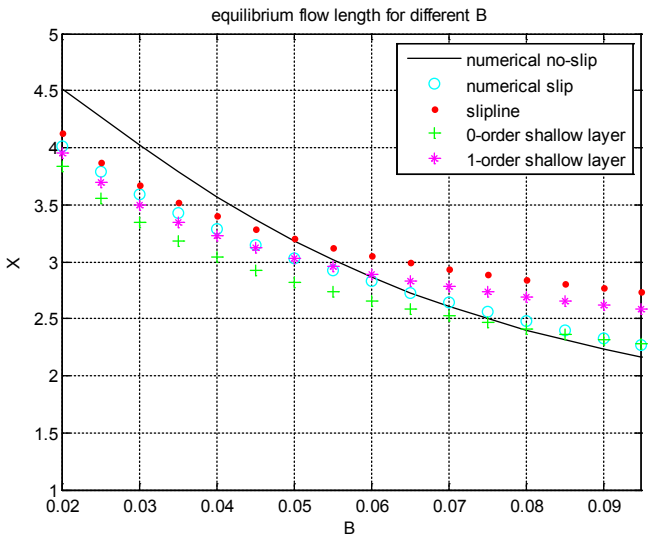

Figure 4.22: equilibrium flow length for B in [0.02 0.1]

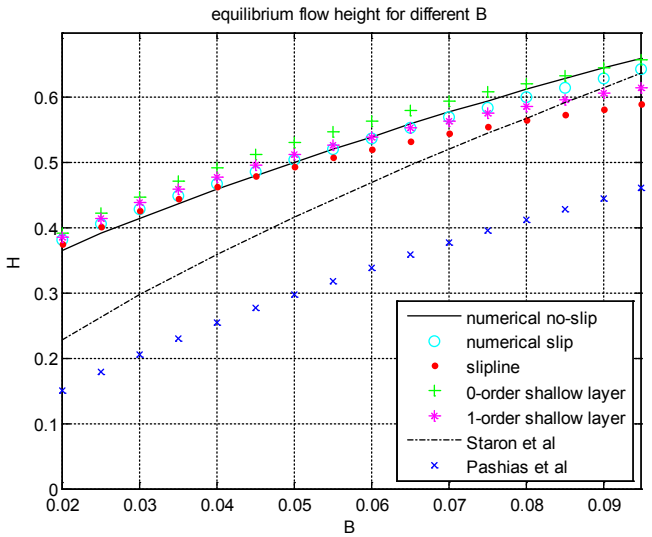

Figure 4.23: equilibrium flow height for B in [0.02 0.1]

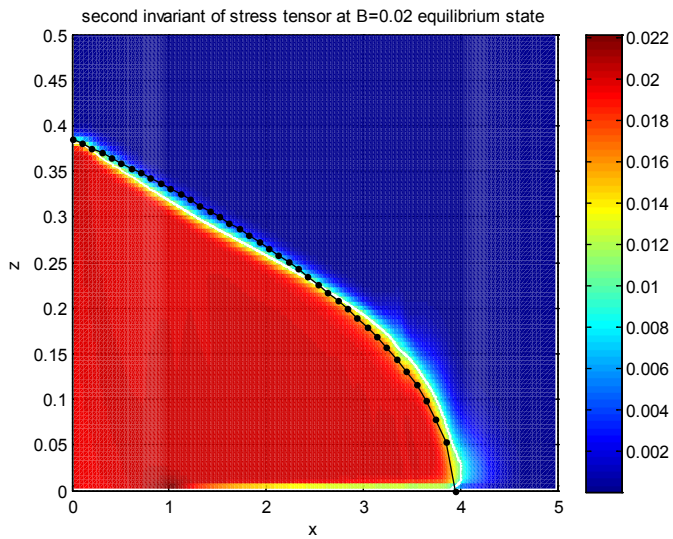

Figure 4.24: The color contour map is the stress field of the equilibrium state for B=0.02, the black curve is the 1-order shallow layer model

are valid for $B \ll 1$. Figure 4.24 is the equilibrium state for $B = 0.02$, the black curve is the 1-order shallow layer model. They correspond well with each other. We can also see from the stress field that the fluid yields everywhere and the stress falls to the dimensionless yield stress B as it reaches the equilibrium. From Figure 4.23, both Staron and Pashias' models are not in a good comparison with the numerical results or the lubrication theory. Pashias' model is different mainly because they assume the equilibrium state has a larger aspect ratio, while in our problem it is small. Staron's model is different because they assume that the slump height is linearly dependent on the initial aspect ratio, for a constant B, and derive that the equilibrium flow height is on the order of $O(B^{2/3})$, while this is not true in the shallow layer model($O(B^{1/3})$), which is more close to the numerical results. For B in [0.1 0.2], the equilibrium spreading length and height are shown in Figure 4.25 and 4.26. There is no big difference between the no-slip model and the slip model. And also the numerical results deviate from both the shallow layer model and other models. This is because B is not small enough, and

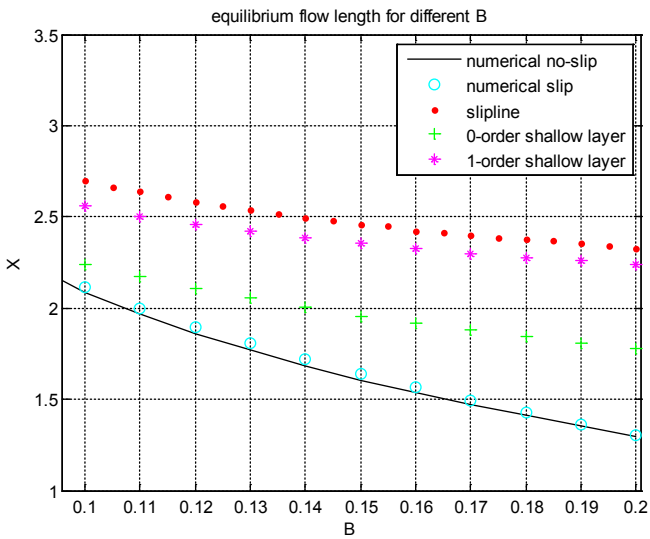

Figure 4.25: equilibrium flow length for B in [0.1 0.2]

some region is not yielded. For example, Figure 4.27 is the stress field of $B = 0.2$ at equilibrium state, the white curve is the final shape predicted by the slipline model, we can see clearly that, at the right-upper corner, there is an unyielded region, which makes the flow spread less than expected.

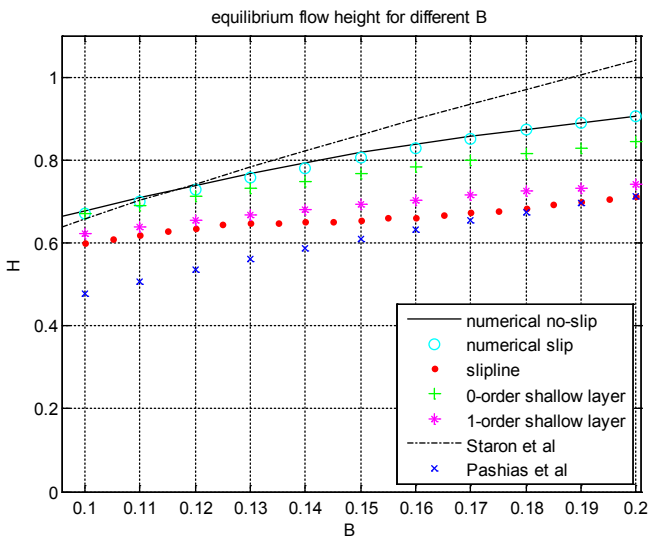

Figure 4.26: equilibrium flow height for B in [0.1 0.2]

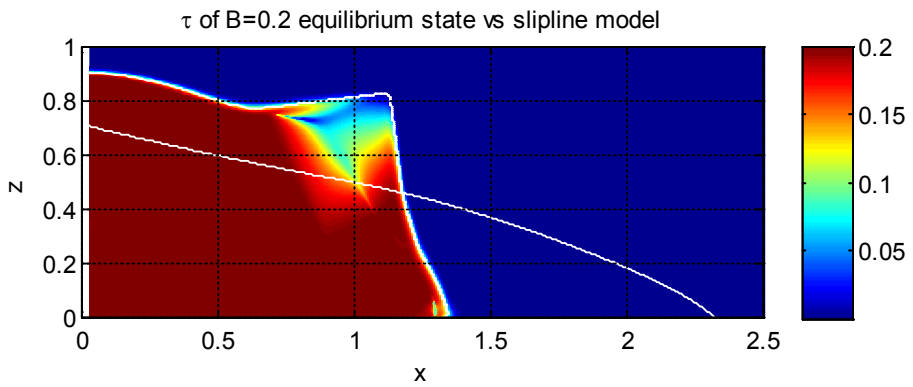

Figure 4.27: The color contour map is the stress field of the equilibrium state for B=0.2, the white curve is the slipline result

Chapter 5

Conclusion

We have performed numerical simulations for a two-layer fluid problem, using a VOF method for the evolution of the fluid and a regularization method for the constitutive law of Bingham fluid, in order to simulate the propagation of the Bingham fluid gravity current.

A Newtonian fluid problem is solved first to validate the code. A resolution problem caused by the no-slip boundary condition is found, due to the appearance of a thin finger of upper layer fluid that is over-ridden by the lower fluid. We are not sure if the finger is physically reasonable or not. If it really exists, it probably requires much higher resolution to be recovered, or demands more than macro-scale fluid dynamics to be understood. Therefore, we consider the possibility that the finger is a numerical effect from the no-slip condition and needs to be removed. A slip boundary condition is shown to remove the finger formed by the upper fluid, thereby avoiding numerical resolution issues. However, we are not convinced that the numerical simulation with a slip boundary condition, is still our original problem(with no-slip condition). So far as we achieved, the slip model is proved to make the result independent of resolution, and it performs better than the no-slip condition results, in comparison with the asymptotic models. Those observations, may imply that the slip condition is an alternative of no-slip condition in numerical simulation of two-layer fluid moving on the wall. Further investigation is still needed.

The slip boundary condition is then used for the Bingham fluid problem. The numerical results for the Bingham fluid problem agree with the asymptotic models for $B < 0.05$, for $B > 0.1$, they become different, as there is genuine unyielded region on the upper-right corner of the fluid. and the final shapes are totally different. As $B > 0.28$, the fluid is always static.

Therefore, we numerically confirm the validity of the shallow layer theory in certain parameter regimes.

Although the numerical simulations agree with the asymptotic results, we are not very confident with the numerical result because the mechanism behind imposing a slip condition is not yet understood, and we are not sure if the modified slip condition $u = \frac{1-c}{c}\Delta y \frac{\partial u}{\partial y}$ is a proper choice(There is a problem caused by imposing the slip-condition in the Bingham fluid problem. Details can be found in Appendix.A.). In fact, it is a common problem that no-slip condition poses a problem in viscous flow theory at contact lines: places where an interface between two fluids meets a solid boundary. Here, the no-slip boundary condition implies that the position of the contact line does not move, which is not observed in reality. Analysis of a moving contact line with the no slip condition demands infinite stresses.

Our next step includes: extending our simulation to an axisymmetric context, and varying the initial shape and aspect ratio and application of the augmented Lagrangian method. We hope to make use of both experiments and large number of numerical simulations to address the finger problem. If the finger is not observed in experiments, that means it is simply a numerical artefact, then the slip model can be validated by comparison with no-slip asymptotic model and experiments, in different contexts.

Bibliography

[1] S.G.Bankoff A.Oron, S.H.Davis. Long scale evolution of thin liquid films. *Reviews of Modern Physics*, 69(3):931, 1997.

[2] F. Necker C. Hartel, E. Meiburg. Analysis and direct numerical simulation of the flow at a gravity-current head. part 1. flow topology and front speed for slip and no-slip boundaries. *J. Fluid Mech.*, 2000.

[3] Kenneth S. Breuer Chang-Hwan Choi, K. Johan A. Westin. Apparent slip flows in hydrophilic and hydrophobic microchannels. *Physics of Fluids*, 15(10), 2003.

[4] J.C. Latche D. Vola, L. Boscardin. Laminar unsteady flows of bingham fluids: a numerical strategy and some benchmark results. *Journal of Computational Physics*, 2003.

[5] L. Preziosi E. Bovet, B. Chiaia. A new model for snow avalanche dynamics based on bingham fluids. *Meccanica*, 45:753–765, 2010.

[6] Giovanna Guidoboni Edward J. Dean, Roland Glowinski. On the numerical simulation of bingham visco-plastic flow: Old and new results. *J. Non-Newtonian Fluid Mech*, 142:36–62, 2007.

[7] H.E.Huppert. The propagation of two-dimensional and axisymmetric viscous gravity currents over a rigid horizontal surface. *J. Fluid Mech.*, 121:43–58, 1982.

[8] C. W. Hirt and B. D. Nichols. Volume of fluid (vof) method for the dynamics of free boundaries. *JOURNAL OF COMPUTATIONAL PHYSICS*, 39:201–225, 1981.

[9] N.J.Balmforth I.J.Hewitt. Viscoplastic lubrication theory with application to bearings and the washboard instability of a planing plate. *J. Non-Newtonian Fluid Mech.*, 2012.

[10] Y.F.Yap J.Liu, N.T.Nguyen. Numerical studies of sessile droplet shape with moving contact lines. *Micro and Nanosystems*, 2011.

[11] I.A. Frigaard K. Wielage-Burchard. Static wall layers in plane channel displacement flows. *Journal of Non-Newtonian Fluid Mechanics*, 2011.

[12] C.C.Mei K.F.Liu. Approximate equations for the slow spreading of a thin sheet of bingham plastic fluid. *Physics of Fluids A: Fluid Dynamics*, 2:30, 1990.

[13] D. Kuzmin. On the design of general-purpose flux limiters for finite element schemes. i. scalar convection. *Journal of Computational Physics*, 219:513–531, 2006.

[14] B.van Leer. Towards the ultimate conservative difference scheme. v.a second-order sequel to godunov's method. *Journal of Computational Physics*, 142(1):101–136, 1979.

[15] P.Ray S.Popinet L.Staron, P.Lagree. Scaling laws for the slumping of a bingham plastic fluid. *J. Rheol.*, 2013.

[16] Evan Mitsoulis. Flows of viscoplastic materials: models and computations. *Rheology Reviews*, pages 135–178, 2007.

[17] J.Li M.Renardy, Y.Renardy. Numerical simulation of moving contact line problems using a volume-of-fluid method. *Journal of Computational Physics*, 171:243–263, 2001.

[18] P. Perona A. C. Rust R. Sassi N. J. Balmforth, R. V. Craster. Viscoplastic dam breaks and the bostwick consistometer. *Journal of Non-Newtonian Fluid Mechanics*, 142:63–78, 2007.

[19] P. Coussot N. Roussel. fifty-cent rheometer for yield stress measurements: From slump to spreading flow. *Journal of Rheology*, 49:705, 2005.

[20] A.C.Slim S.Cochard N.Dubash, N.J.Balmforth. What is the final shape of a viscoplastic slump? *J. Non-Newtonian Fluid Mech.*, 158:91–100, 2009.

[21] R. Sassi N.J. Balmforth, R.V. Craster. Shallow viscoplastic flow on an inclined plane. *J. Fluid Mech.*, 470:1–29, 2002.

[22] A.C.Rust R.Sassi N.J.Balmforth, R.V.Craster. Viscoplastic flow over an inclined surface. *J.Non-Newtonian Fluid Mech.*, 142:219–243, 2007.

[23] J.Summers D.J.Glenister N.Pashias, D.V.Boger. A fifty cent rheometer for yield stress measurement. *Journal of Rheology*, 1996.

[24] C. Ancey S. Cocharda. Experimental investigation of the spreading of viscoplastic fluids on inclined planes. *Journal of Non-Newtonian Fluid Mechanics*, 158:73–84, 2009.

[25] I. A. Frigaard S. Hormozi, K.Wielage-Burchard. Entry and start up effects in visco-plastically lubricated viscous shear flow in pipe. *Journal of Fluid Mechanics*, 673:432–467, 2011.

[26] S.G.Mikhlin. *Variational methods in Mathematical Physics*. Pergamon Press, 1964.

Appendix A

Code Validation

A.1 The results are independent of tolerance

The convergence criteria for solving the Navier-Stokes equations is when tolerance $tol > \max(||\nabla \cdot u||, ||u^{n+1} - u^n||)$. We test the $tol = 10^{-6}, 10^{-8}$ to see if the results are different, Figure A.1 and A.2 are the plots for the evolution of flow height and length, for the two tolerance(with all other settings the same). It shows that $tol = 10^{-6}$ is enough for convergence.

A.2 The results are independent of time step

It is necessary to show that the time step ΔT for each iterations of Navier-Stokes solver is small enough so that the velocity during any time is well captured. The time step here is set to be $0.5, 0.25, 0.125$, with all other settings the same. Figure A.3 and A.4 are the results. It shows that $\Delta T = 0.5$ is small enough.

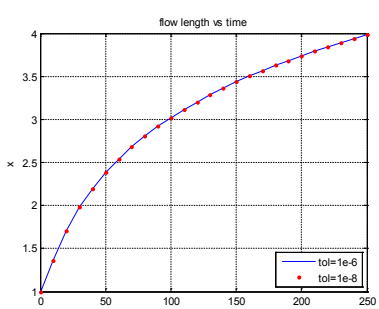

Figure A.1: x vs t for different tolerance

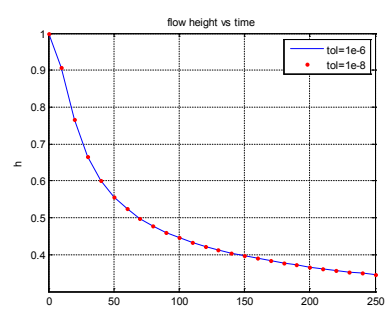

Figure A.2: h vs t for different tolerance

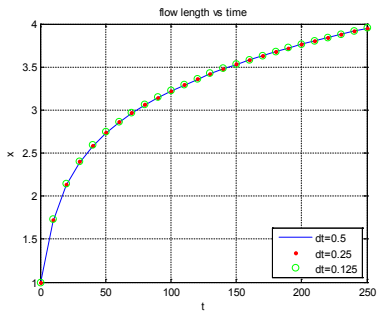

Figure A.3: x vs t for different time step

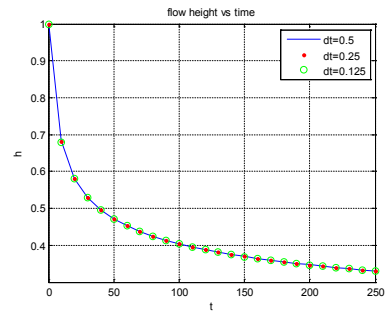

Figure A.4: h vs t for different time step

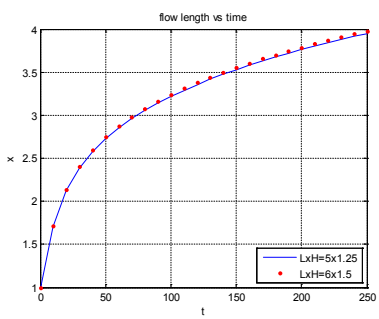

Figure A.5: x vs t for different domain size

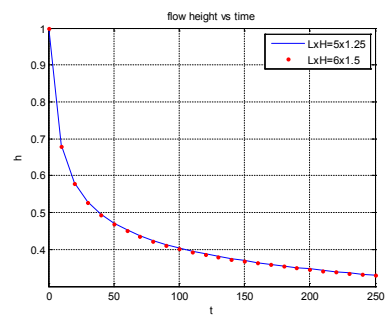

Figure A.6: h vs t for different domain size

A.3 The domain size

Since we want to make the effect of the upper layer as small as possible, it is necessary to make sure that the change in domain size will not lead to a big difference in the result. We choose $L \times H = 5 \times 1.25,\ 6 \times 1.5$, while the initial size of the lower layer is still 1×1. Figure A.5 and A.6 are the results. It shows that the effect of the domain size is small enough, thus we choose $L \times H = 5 \times 1.25$ as the standard setting in our problem.

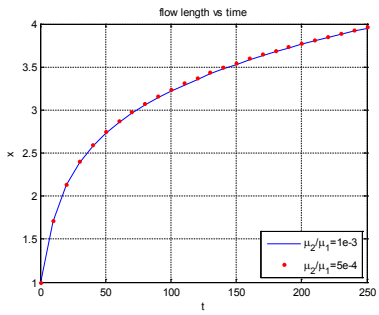

Figure A.7: x vs t for different viscosity ratio

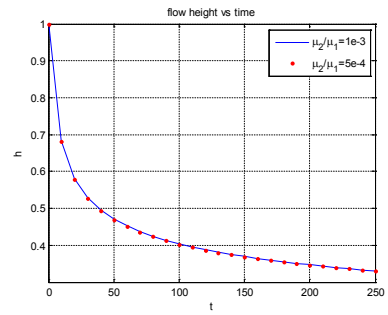

Figure A.8: h vs t for different viscosity ratio

A.4 The density and viscosity ratio

For the same reason as the domain size test, it is necessary to show that the change in density and viscosity ratio will not leading to big difference in the results. We make the viscosity ratio $\frac{\mu_2}{\mu_1} = 10^{-3}, 5 \times 10^{-4}$, with all other settings the same. Figure A.7 and A.8 show the results. It implies that $\frac{\mu_2}{\mu_1} = 10^{-3}$ is small enough to make the results independent of the upper layer.

A.5 Reynolds number

For Bingham fluid, the inertial force sometimes can change the equilibrium shape. To avoid the effect of inertia, it is necessary to make sure that the Reynolds number is small enough, so that the Bingham fluid propagation is not affected by inertia. We do computations for $Re = 9.81 \times 10^{-4}, 7.85 \times 10^{-3}$, Figure A.9 and A.10 are the results. It shows that the inertia can be neglected.

A.6 Regularization parameter is small enough

The regularization parameter ϵ of the model $\tau = (1 + \frac{B}{\gamma+\epsilon})\gamma$ needs to be small enough so that it has no effect on the propagation of Bingham fluid

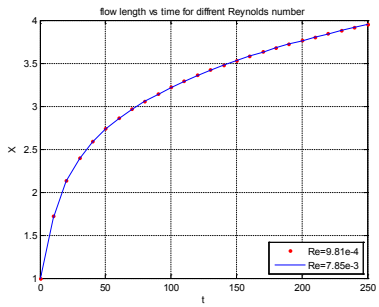

Figure A.9: x vs t for different Reynolds number

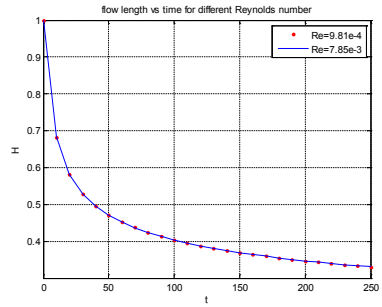

Figure A.10: h vs t for different Reynolds number

before stopping. We did a test by setting $B = 0.04$, and $\epsilon = 10^{-4}$ to 10^{-8}, with all other settings the same. It indicates that as $\epsilon \leq 10^{-6}$, there is no difference in the results. To make the effect small enough, ϵ is always chosen to be 10^{-8} in our tests.

A.7 Problems with the slip boundary condition

Figure A.11 compares the flow evolution of the two types of boundary conditions for $B = 0.1$. We can see that, before reaching the equilibrium, the slip model spreads more slowly than the no-slip one. However, around the equilibrium, the no-slip model stops right away, while the slip model continues to spread. The observation above implies that the modified slip model is invalid around the equilibrium. It needs to be corrected to address this issue. Therefore, the no-slip model is a relatively more valid model for B in [0.1 0.2], as there is not much of a finger. This observation reflects the deficiency of slip condition in Bingham fluid problem, as we cannot tell if the flow really stops at the equilibrium, which implies that the slip model is not a proper choice in this Bingham fluid problem. One way of resolving this is to use the stopping time from the no-slip results.

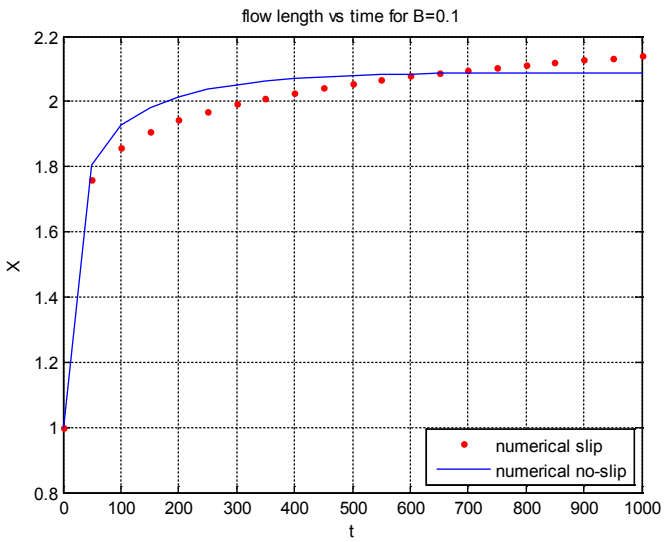

Figure A.11: flow length vs time for different BCs